



<b>Publication Year</b>	2016
<b>Acceptance in OA @INAF</b>	2020-05-13T09:30:22Z
<b>Title</b>	The VIMOS Public Extragalactic Redshift Survey (VIPERS). Environmental effects shaping the galaxy stellar mass function
<b>Authors</b>	Davidzon, I.; CUCCIATI, Olga; BOLZONELLA, MICOL; DE LUCIA, GABRIELLA; Zamorani, G.; et al.
<b>DOI</b>	10.1051/0004-6361/201527129
<b>Handle</b>	<a href="http://hdl.handle.net/20.500.12386/24781">http://hdl.handle.net/20.500.12386/24781</a>
<b>Journal</b>	ASTRONOMY & ASTROPHYSICS
<b>Number</b>	586

# The VIMOS Public Extragalactic Redshift Survey (VIPERS)

## Environmental effects shaping the galaxy stellar mass function<sup>\*</sup>

I. Davidzon<sup>1,2</sup>, O. Cucciati<sup>3,2</sup>, M. Bolzonella<sup>2</sup>, G. De Lucia<sup>4</sup>, G. Zamorani<sup>2</sup>, S. Arnouts<sup>1,5</sup>, T. Moutard<sup>1</sup>, O. Ilbert<sup>1</sup>, B. Garilli<sup>6</sup>, M. Scodeggio<sup>6</sup>, L. Guzzo<sup>7,8</sup>, U. Abbas<sup>9</sup>, C. Adami<sup>1</sup>, J. Bel<sup>7,10,11</sup>, D. Bottini<sup>6</sup>, E. Branchini<sup>12,13,14</sup>, A. Cappi<sup>2,15</sup>, J. Coupon<sup>16</sup>, S. de la Torre<sup>1</sup>, C. Di Porto<sup>2</sup>, A. Fritz<sup>6</sup>, P. Franzetti<sup>6</sup>, M. Fumana<sup>6</sup>, B. R. Granett<sup>7</sup>, L. Guennou<sup>17,1</sup>, A. Iovino<sup>7</sup>, J. Krywult<sup>18</sup>, V. Le Brun<sup>1</sup>, O. Le Fèvre<sup>1</sup>, D. Maccagni<sup>6</sup>, K. Malek<sup>19</sup>, F. Marulli<sup>3,2,20</sup>, H. J. McCracken<sup>21</sup>, Y. Mellier<sup>21</sup>, L. Moscardini<sup>3,2,20</sup>, M. Polletta<sup>6</sup>, A. Pollo<sup>22,19</sup>, L. A. M. Tasca<sup>1</sup>, R. Tojeiro<sup>23</sup>, D. Vergani<sup>24,2</sup>, and A. Zanichelli<sup>25</sup>

(Affiliations can be found after the references)

Received 5 August 2015 / Accepted 2 November 2015

### ABSTRACT

We exploit the first public data release of VIPERS to investigate environmental effects in the evolution of galaxies between  $z \sim 0.5$  and  $0.9$ . The large number of spectroscopic redshifts (more than 50 000) over an area of about  $10 \text{ deg}^2$  provides a galaxy sample with high statistical power. The accurate redshift measurements ( $\sigma_z = 0.00047(1 + z_{\text{spec}})$ ) allow us to robustly isolate galaxies living in the lowest and highest density environments ( $\delta < 0.7$  and  $\delta > 4$ , respectively) as defined in terms of spatial 3D density contrast  $\delta$ . We estimate the stellar mass function of galaxies residing in these two environments and constrain the high-mass end ( $M \gtrsim 10^{11} M_\odot$ ) with unprecedented precision. We find that the galaxy stellar mass function in the densest regions has a different shape than was measured at low densities, with an enhancement of massive galaxies and a hint of a flatter (less negative) slope at  $z < 0.8$ . We normalise each mass function to the comoving volume occupied by the corresponding environment and relate estimates from different redshift bins. We observe an evolution of the stellar mass function of VIPERS galaxies in high densities, while the low-density one is nearly constant. We compare these results to semi-analytical models and find consistent environmental signatures in the simulated stellar mass functions. We discuss how the halo mass function and fraction of central/satellite galaxies depend on the environments considered, making intrinsic and environmental properties of galaxies physically coupled, hence difficult to disentangle. The evolution of our low-density regions is described well by the formalism introduced by Peng et al. (2010, ApJ, 721, 193), and is consistent with the idea that galaxies become progressively passive because of internal physical processes. The same formalism could also describe the evolution of the mass function in the high density regions, but only if a significant contribution from dry mergers is considered.

**Key words.** galaxies: evolution – galaxies: statistics – galaxies: interactions – large-scale structure of Universe

## 1. Introduction

Several decades after the pioneering work of Oemler (1974), Davis & Geller (1976), and Sandage & Visvanathan (1978), the role of environment in driving galaxy evolution still represents a research frontier. Several correlations have been observed between the place in which galaxies reside and their own properties (see e.g. Blanton & Moustakas 2009, for a review), but the mechanisms responsible for them remain poorly understood. Even the well-established morphology-density relation (Dressler 1980; Postman & Geller 1984) has a number of contrasting

interpretations (cf. Thomas et al. 2010; van der Wel et al. 2010; Cappellari et al. 2011).

Many pieces of evidence suggest that the environment has a fundamental influence (e.g. Cooper et al. 2008; Cucciati et al. 2010; Burton et al. 2013). In particular, some of the processes halting the production of new stars (the so-called “galaxy quenching”) should be related to the dense intergalactic medium (e.g. ram pressure stripping) and/or interactions with nearby galaxies (for more details, see e.g. Boselli & Gavazzi 2006; Gabor et al. 2010; Woo et al. 2012). In contrast, other authors consider the galaxy stellar mass ( $M$ ) or the halo mass ( $M_h$ ) to be the main evolutionary drivers with a secondary – or even negligible – contribution by their environment (e.g. Pasquali et al. 2009; Thomas et al. 2010; Grützbauch et al. 2011).

Classical discussions contrast a scenario in which the fate of a galaxy is determined primarily by physical processes coming into play after the galaxy has become part of a group or of a cluster (“nurture”) to one in which the observed environmental trends are established before these events and primarily determined by internal physical processes (“nature”). However, this dichotomy is simplistic because stellar mass and environment are inter-related. In fact, the parametrisation of the latter is often connected to the gravitational mass of the hosting halo, which

<sup>\*</sup> Based on observations collected at the European Southern Observatory, Cerro Paranal, Chile, using the Very Large Telescope under programmes 182.A-0886 and partly 070.A-9007. Also based on observations obtained with MegaPrime/MegaCam, a joint project of CFHT and CEA/DAPNIA, at the Canada-France-Hawaii Telescope (CFHT), which is operated by the National Research Council (NRC) of Canada, the Institut National des Sciences de l’Univers of the Centre National de la Recherche Scientifique (CNRS) of France, and the University of Hawaii. This work is based in part on data products produced at TERAPIX and the Canadian Astronomy Data Centre as part of the Canada-France-Hawaii Telescope Legacy Survey, a collaborative project of NRC and CNRS.

is also physically coupled to galaxy stellar mass. Therefore, in a scenario of hierarchical accretion, it is expected that most massive galaxies show a correlation with overdensities (Kauffmann et al. 2004; Abbas & Sheth 2005; Scodeggio et al. 2009). For this reason, it is misleading to contrast stellar mass and environment as two separate aspects of galaxy evolution (see the discussion in De Lucia et al. 2012).

Another crucial point is how the environment is defined. One possibility is to identify high-density regions as galaxy groups and clusters, in contrast to a low-density field, which is sometimes ambiguously defined. When halo mass estimates are used, the classification is more tightly related to the underlying distribution of dark matter, with galaxies often divided into satellite and central objects (van den Bosch et al. 2008). Other methods, involving galaxy counts, can identify a broad range of densities with a resolution from a few Megaparsecs down to  $\sim 100$  kpc. These methods are based on the two-point clustering (e.g. Abbas & Sheth 2005), Voronoi’s tessellation (e.g. Marinoni et al. 2002), or the computation of the galaxy number density inside a window function, which is the approach used in the present work. In general, different methods probe galaxy surroundings on different scales (Mulder et al. 2012). Nonetheless, the method we adopt here (based on the fifth nearest neighbourhood) is expected to be in overall good agreement with other robust estimators, such as Delaunay’s or Voronoi’s tessellations (see Darvish et al. 2015).

In this kind of research, the galaxy stellar mass function (GSMF) is one of the most effective tools. Especially when computed inside a specific environment, the GSMF requires excellent data derived from the observation of wide fields or a large number of clusters or groups. For this reason, only a few studies of the GSMF consider the environmental dependence aspects (e.g. Baldry et al. 2006; Bundy et al. 2006; Bolzonella et al. 2010; Vulcani et al. 2012; Giodini et al. 2012; Annunziatella et al. 2014; Hahn et al. 2015; Mortlock et al. 2014). Although still fragmentary, an interesting picture is emerging from this work. In the local Universe, Baldry et al. (2006, SDSS data) observe a correlation between the turn-off mass of the GSMF ( $M_*$ ) and the local density (which they estimate as an average between the fourth and fifth nearest neighbours). In the lowest densities, they estimate  $\log(M_*/M_\odot) \simeq 10.6$ , reaching values of about 11.0 in the densest environment. Probing a wider redshift range (from  $z \sim 1$  to  $\sim 0.1$ ), Bolzonella et al. (2010) detect environmental effects for zCOSMOS (Lilly et al. 2007) galaxies: the passive population grows more rapidly inside regions of high density (recovered by counting the fifth nearest neighbour of each galaxy). The authors find this trend by studying the redshift evolution of  $M_{\text{cross}}$ , i.e. the value of stellar mass at which the active and passive GSMFs intersect each other (see also Bundy et al. 2006; Peng et al. 2010; Annunziatella et al. 2014).

Recent studies indicate that already at  $z \sim 1$ , the assembly of massive galaxies is faster in overdensities (Mortlock et al. 2014). Using a slightly different classification with respect to Bolzonella et al., i.e. relying on the third nearest neighbour, Bundy et al. (2006) seek environmental effects in the stellar mass function of DEEP2 galaxies from  $z = 0.4$  to 1.4. The evolution they find shows a mild dependence on local environment, such that Bundy et al. quantify it as a secondary driver with respect to stellar mass. Other studies compare the stellar mass functions of clusters, groups, and isolated (or “field”) galaxies. Using the 10k zCOSMOS sample, Kovač et al. (2010b) confirm the trend noted by Bolzonella et al. (2010): massive galaxies tend to reside inside groups. Annunziatella et al. (2014)

find that the passive galaxy stellar mass function in a cluster of the CLASH-VLT survey has a steeper slope in the core of the cluster than in the outskirts (see also Annunziatella et al. 2016). On the other hand, Calvi et al. (2013) and Vulcani et al. (2012, 2013) compare galaxy clusters and the general field up to  $z \simeq 0.8$ , without detecting any significant difference in the respective GSMFs. van der Burg et al. (2013) also find similar shapes for active and passive mass functions in each environment, although the total GSMFs differ from each other because of the different percentage of passive galaxies in their clusters at  $0.86 < z < 1.34$  with respect to the field. We note, however, that these analyses are based on different kinds of datasets: Vulcani et al. and van der Burg et al. use samples of several clusters, while Annunziatella et al. focus on one system but with deeper and wider observations.

We aim to provide new clues in this context, exploiting the VIMOS Public Extragalactic Redshift Survey (VIPERS, Guzzo et al. 2014) to search for environmental effects between  $z \simeq 1$  and  $z \simeq 0.5$ . As shown in a previous paper of this series (Davidzon et al. 2013, hereafter D13), the VIPERS data allow robust measurement of the GSMF. The accurate VIPERS redshifts are also the cornerstone for estimating the local density contrast around each galaxy. This task was carried out in Cucciati et al. (2014) and will be further developed in another study focused on the colour-density relation (Cucciati et al., in prep.). In the present paper, Sect. 2 contains a general description of the survey. The computation of local density contrast is summarised in the same section, along with deriving other fundamental galaxy quantities (in particular galaxy stellar mass). In Sect. 3 we present our classification of environment and galaxy types. After posing these definitions, we are able to estimate the GSMF in low- and high-density regions of VIPERS, also considering the passive and active galaxy samples separately (Sect. 4). The interpretation of our results is discussed in Sect. 5, while conclusions are in Sect. 6.

Our measurements assume a flat  $\Lambda$ CDM cosmology in which  $\Omega_m = 0.25$ ,  $\Omega_\Lambda = 0.75$ , and  $h_{70} = H_0/(70 \text{ km s}^{-1} \text{ Mpc}^{-1})$ , unless specified otherwise. Magnitudes are in the AB system (Oke 1974).

## 2. Data

Since 2008, VIPERS has probed a volume of  $\sim 1.5 \times 10^8 \text{ Mpc}^3 h_{70}^{-3}$  between  $z = 0.5$  and 1.2, providing the largest spectroscopic galaxy catalogue at intermediate redshifts. The final public release, expected in 2016, will cover  $24 \text{ deg}^2$ , including about 90 000 galaxies and AGNs in the magnitude range of  $17.5 \leq i \leq 22.5$ . The first public data release (PDR1), consisting of 57 204 spectroscopic measurements, has been presented in Garilli et al. (2014) and is now available on the survey database<sup>1</sup>.

From a cosmological perspective, the main goal of VIPERS is to measure the growth rate of structure (de la Torre et al. 2013). Additional science drivers also refer to extragalactic research fields, to investigate a wide range of galaxy properties at an epoch when the Universe was about half its current age (Marchetti et al. 2013; Malek et al. 2013; D13; Fritz et al. 2014). In addition, in the context of the present study, it is worth mentioning the VIPERS papers that describe the relation between baryons and dark matter through the galaxy bias factor (Marulli et al. 2013; Di Porto et al. 2014; Cappi et al. 2015; Granett et al. 2015). Both the galaxy density field and the galaxy bias, if the

<sup>1</sup> <http://vipers.inaf.it/rel-pdr1.html>

latter is measured as a function of stellar mass and/or luminosity, are intimately linked to clustering and the total matter distribution. We refer the reader to [Guzzo et al. \(2014\)](#) and [Garilli et al. \(2014\)](#) for further details on the survey construction and the scientific investigations being carried out by the VIPERS collaboration.

### 2.1. Photometry

The spectroscopic survey is associated with photometric ancillary data obtained from both public surveys and dedicated observations. The VIPERS targets have been selected within two fields of the Canada-France-Hawaii Telescope Legacy Survey Wide (CFHTLS-Wide<sup>2</sup>), namely W1 and W4. The CFHTLS optical magnitudes were derived by the Terapix team<sup>3</sup> by means of SExtractor (MAG\_AUTO in double image mode, see [Bertin & Arnouts 1996](#)) in the filters  $u^*$ ,  $g'$ ,  $r'$ ,  $i'$ , and  $z'$ . Photometric redshifts ( $z_{\text{phot}}$ ) have been estimated by using these magnitudes, following the procedure described in [Coupon et al. \(2009\)](#); their uncertainty is  $\sigma_{z_{\text{phot}}} = 0.035(1 + z_{\text{phot}})$ . This photometric catalogue is limited at  $i \leq 22.5$ , and we refer to it as the “parent sample” of VIPERS. Sources whose quality was deemed insufficient for our analysis (e.g. because of nearby stars) have been excluded by means of angular masks.

Beyond optical data, a  $K_s$ -band follow-up added information in the near-infrared (NIR) range. Data were collected by means of the WIRCam instrument at CFHT, setting an optimised depth to match the brightness of the spectroscopic sources (Moutard et al., in prep.). These observations cover the W4 field almost completely, while a  $1.6 \times 0.9 \text{ deg}^2$  area is missing in W1 (see D13, Fig. 1). At  $K \leq 22.0$  (that is the  $5\sigma$  limiting magnitude), 96% of the VIPERS objects in W4 have a WIRCam counterpart, as compared to 80% in W1. When estimating galaxy stellar masses by fitting galaxy spectral energy distributions (SEDs), NIR photometry can be critical, for example, to avoid age underestimates (see [Lee et al. 2009](#)). For this reason,  $K_{\text{WIRCam}}$  has been complemented by the UKIDSS data<sup>4</sup>. The sky region that WIRCam did not observe in W1 is fully covered by the UKIDSS-DXS survey, which has been used also in W4 – together with the shallower UKIDSS-LAS – for fewer than 300 sparse objects not matched with  $K_{\text{WIRCam}}$ . After that, the fraction of our spectroscopic sample having  $K$ -band magnitude rises to 97% both in W1 and in W4. In the absence of  $K$  magnitudes, we use (where possible) the  $J$  band from UKIDSS. The comparison between  $K_{\text{WIRCam}}$  and  $K_{\text{UKIDSS}}$  was performed in D13: the two surveys are in good agreement, and we can safely combine them.

In addition, about 32% of the spectroscopic targets in W1 lie in the XMM-LSS field and have been associated with infrared (IR) sources observed by SWIRE<sup>5</sup>. Since our SED fitting (Sect. 2.3) uses models of stellar population synthesis that do not reproduce the re-emission from dust, we only considered magnitudes in the  $3.6 \mu\text{m}$  and  $4.5 \mu\text{m}$  bands. It should be also noticed that beyond those wavelengths SWIRE is shallower, and source detection is very sparse.

### 2.2. Spectroscopy

We extract our galaxy sample from the same spectroscopic catalogue as used in D13. That catalogue includes 53 608 galaxy spectra with  $i \leq i_{\text{lim}} \equiv 22.5$ . Along with the limiting magnitude, an additional criterion for target selection, based on  $(g - r)$  and  $(r - i)$  colours, was successfully applied to enhance the probability of observing galaxies at  $z > 0.5$  (see [Guzzo et al. 2014](#)).

Spectra were observed at VLT using the VIMOS multi-object spectrograph ([Le Fèvre et al. 2003](#)) with the LR-Red grism ( $R = 210$ ) in a wavelength range of 5500–9500 Å. The four quadrants of the VIMOS instrument, separated by gaps that are  $2'$  wide, produce a characteristic footprint that we have accounted for by means of spectroscopic masks. Besides gaps, a few quadrants are missing in the survey layout ([Guzzo et al. 2014](#), Fig. 10) because of technical problems in the spectrograph set-up. After removing the vignetted parts of each pointing, the effective area covered by the survey is 5.34 and 4.97  $\text{deg}^2$  in W1 and W4, respectively. To maximise the number of targets, we used short slits as proposed in [Scodeggio et al. \(2009\)](#). As a result, we targeted ~45% of the available sources in a single pass.

A description of the VIPERS data reduction can be found in [Garilli et al. \(2012\)](#). At the end of the pipeline, a validation process was carried out by team members, who checked the measured redshifts and assigned a quality flag ( $z_{\text{flag}}$ ) to each of them. Such a flag corresponds to the confidence level (CL) of the measurement, according to the same scheme as adopted by previous surveys like VVDS ([Le Fèvre et al. 2005](#)) and zCOSMOS. The sample we use includes galaxies with  $2 \leq z_{\text{flag}} \leq 9$ , corresponding to 95% CL. It comprises 34 571 spectroscopic measurements between  $z = 0.5$  and 0.9, i.e. the redshift range of the present analysis. We estimate the error in the  $z_{\text{spec}}$  measurements from repeated observations. It is  $\sigma_z = 0.00047(1 + z_{\text{spec}})$ , corresponding to a velocity uncertainty of  $\sim 140 \text{ km s}^{-1}$  ([Guzzo et al. 2014](#)). We provide each object with a statistical weight  $w(i, z)$  to make this sample representative of all the photometric galaxies at  $i < 22.5$  in the survey volume. We estimate weights by considering three selection functions: the target sampling rate (TSR), the spectroscopic success rate (SSR), and the colour sampling rate (CSR). Further details about TSR, SSR, and CSR are provided in [Fritz et al. \(2014\)](#), [Guzzo et al. \(2014\)](#), and [Garilli et al. \(2014\)](#). The overall sampling rate, i.e.  $\text{TSR} \times \text{SSR} \times \text{CSR}$ , is on average 35%.

### 2.3. SED fitting estimates

We estimate several quantities, in particular galaxy stellar masses and absolute magnitudes, by means of SED fitting, in a similar way to D13. Through this technique, physical properties of a given galaxy can be derived from the template (i.e. the synthetic SED) that reproduces its multi-band photometry best (after redshifting the template to  $z = z_{\text{spec}}$  or  $z_{\text{phot}}$ ). To this purpose, we use the code *Hyperzmass*, a modified version of *Hyperz* ([Bolzonella et al. 2000](#)) developed by [Bolzonella et al. \(2010\)](#). The software selects the best-fit template as the one that minimises the  $\chi^2$ .

To build our library of galaxy templates we start from the simple stellar populations modelled by [Bruzual & Charlot \(2003\)](#), hereafter BC03). The BC03 model assumes a universal initial mass function (IMF) and a single non-evolving metallicity ( $Z$ ) for the stars belonging to a given simple stellar population (SSP). Many SSPs are combined and integrated in order to reproduce a galaxy SED.

<sup>2</sup> <http://www.cfht.hawaii.edu/Science/CFHLS/>

<sup>3</sup> Data available at <http://www.terapix.iap.fr> (T0005 data release).

<sup>4</sup> <http://www.ukidss.org>, note that Petrosian magnitudes in the database are in Vega system, but conversion factors to AB system are provided by the UKIDSS team on the reference website.

<sup>5</sup> <http://swire.ipac.caltech.edu/swire>



As in D13, we choose SSPs with [Chabrier \(2003\)](#) IMF, having metallicity either  $Z = Z_{\odot}$  or  $Z = 0.2 Z_{\odot}$  to sample the metallicity range observed for galaxies at  $z \sim 0.8$  ([Zahid et al. 2011](#)). We adopt only two values to limit degeneracy with other parameters such as the age. Synthetic galaxy SEDs are derived by evolving the SSPs in agreement with a given star formation history (SFH). We assume eleven SFHs: one with a constant SFR and ten with an exponentially declining profile, i.e.  $SFR \propto \exp(-t/\tau)$  with values of  $\tau$  ranging between 0.1 and 30 Gyr. The formation redshift of our galaxy templates is not fixed, but the ages allowed in the fitting procedure range from 0.09 Gyr to the age of the Universe at the redshift of the fitted galaxy. Composite SFHs could be considered by adding random bursts of star formation to the exponential (or constant) SFR, as in [Kauffmann et al. \(2003\)](#). However, in D13 we checked that replacing smooth SFHs with more complex ones has a critical impact on the stellar mass estimate (i.e., more than 0.3 dex difference) only for a small percentage (<10%) of the VIPERS galaxies, while for the majority of the sample the change is less than  $\sim 0.1$  dex (see also [Pozzetti et al. 2007](#)). Similar conclusions are drawn by [Mitchell et al. \(2013\)](#), who find that the exponential decrease is a reasonable approximation of the true (i.e. composite) SFH of their simulated galaxies: their SED fitting estimates show small scatter and no systematics with respect to the stellar masses obtained from the theoretical model (see also [Ilbert et al. 2013](#), whose results do not change significantly when using either composite or “delayed” SFHs).

Attenuation by dust is modelled by assuming either a [Calzetti et al. \(2000\)](#) or [Prévot-Bouchet \(Prévot et al. 1984; Bouchet et al. 1985\)](#) extinction law. For both, we let the V-band attenuation vary from  $A_V = 0$  (i.e. no dust) to 3 mag with steps of 0.1. No prior is implemented to distinguish between the two extinction laws: for each galaxy the model is chosen that minimises the  $\chi^2$ . We exclude from our library those templates having an unphysical SED, according to observational evidence. Galaxy models with  $\text{age}/\tau > 4$  and  $A_V > 0.6$  are not used in the fitting procedure, since they represent old galaxies with an excessive amount of dust compared to what is observed in the local Universe (cf. [Brammer et al. 2009](#), Fig. 3). We also rule out best-fit solutions representing early-type galaxies (ETGs) with too young ages, i.e. models with  $\tau \leq 0.6$  Gyr and redshift of formation  $z_{\text{form}} < 1$  (evidence of high  $z_{\text{form}}$  of ETGs can be found e.g. in [Fontana et al. 2004; Thomas et al. 2010](#)). Any other combination of parameters within the ranges mentioned above is allowed. Considering all these parameters and their allowed ranges, our SED fitting should provide us with stellar mass estimates with an uncertainty of  $\lesssim 0.3$  dex, according to [Conroy et al. \(2009\)](#). Moreover, we emphasise that the lack of IR photometry for a small part of the VIPERS sample (see Sect. 2.1) does not introduce significant bias, as already tested in D13.

In addition to stellar mass, we estimate absolute magnitudes in several bands from the same best-fit SED. To minimise the model dependency, we take the apparent magnitude in the closest filter to the rest-frame wavelength of interest and apply a k- and colour-correction based on the SED shape. In this way, the outcome is not very sensitive to the chosen template, relying mainly on the observations. When applied to optical/NIR filters, typical uncertainties of this procedure are about 0.05 mag at  $0.5 < z < 0.9$  ([Fritz et al. 2014](#)).

#### 2.4. Galaxy density contrast

To characterise the different environments in which galaxies live (Sect. 3.1), we rely on the galaxy density contrast ( $\delta$ ). This

quantity is related to the local concentration of galaxies (i.e. the galaxy density field  $\rho$ ) and the mean galaxy density ( $\bar{\rho}$ ) such that  $\delta = (\rho - \bar{\rho})/\bar{\rho}$ . Although  $\rho$  is a point field indirectly connected to matter density, it is a good proxy for the underlying matter distribution: through various smoothing schemes (included the one described here), it is possible to recover the latter from the former with a scale-independent bias factor ([Amara et al. 2012; Di Porto et al. 2014](#)). The procedure adopted here is thoroughly described in a companion paper ([Cucciati et al. 2014](#)).

To derive the local density of any given galaxy, we count objects inside a filter centred on it. Those objects that trace  $\rho$  are part of a “volume-limited” sample that includes both spectroscopic and photometric galaxies. The latter ones come from the photometric parent catalogue, which contains CFHTLS sources with the same *i*-band cut of VIPERS (see Sect. 2.1). To build such a sample, we select galaxies in W1 and W4 with  $M_B < -20.4 - Qz$ . The factor  $Q$  takes the evolution in redshift of the characteristic galaxy luminosity into account, as determined by  $M_B^*$  in the galaxy luminosity functions (see more details e.g. in [Moustakas et al. 2013](#)). We set  $Q = 1$  according to the zCOSMOS luminosity function (which encompasses  $z \sim 0.2$  to 0.9, see [Zucca et al. 2009](#)). The volume-limited sample is complete up to  $z = 0.9$  and traces the underlying cosmic structure avoiding strongly evolving bias that instead a flux-limited sample would produce (cf. [Amara et al. 2012](#)). We refer to this volume-limited sample as the sample of “tracers” (to be distinguished from the VIPERS sample for which we compute  $\delta$ ).

Among those tracers, 14 028 objects have a  $z_{\text{spec}}$  with  $z_{\text{flag}} \in [2, 9]$ , while more than 100 000 have a  $z_{\text{phot}}$ . The large number of spectroscopic redshifts – and their accuracy – are crucial for robustly determining the density field in the three-dimensional (redshift) volume: generally, when only using photometric redshifts, the reconstruction along the line of sight is prevented by their larger photo- $z$  errors (e.g. [Cooper et al. 2005; Scoville et al. 2013](#)). We compute  $\delta$  for galaxies beyond  $z = 0.51$ , to avoid the steep decrease in  $N(z)$  at  $z \lesssim 0.5$  (see [Guzzo et al. 2014](#), Fig. 13) that could affect our density estimates.

Thanks to the photometric redshifts, there is also a sufficient number of (photometric) tracers in the gaps produced by the footprint of VIMOS and in the missing quadrants<sup>6</sup>. In the absence of a secure spectroscopic measurement, we apply a modified version of the method described by [Kovač et al. \(2010a\)](#). The key idea of the method is that galaxy clustering along the line of sight, recovered by using spectroscopic redshifts, provides information about the radial positions of a photometric object, i.e. it is likely to lie where the clustering is higher. Thus, to each photometric tracer we assign a distribution of  $z_{\text{peak}}$  values, together with an ensemble of statistical weights. For each value of  $z_{\text{peak}}$ , the associated weight  $w_{\text{peak}}$  represents the relative probability for the object to be at that given redshift (the sum of weights is normalised to unity). In other words, the  $z_{\text{peak}}$  values are the “most likely” radial positions of a photometric tracer.

In detail, to determine  $z_{\text{peak}}$  and  $w_{\text{peak}}$ , we proceed as follows. We start from the probability distribution function (PDF) of the measured  $z_{\text{phot}}$ , assumed to be a Gaussian with rms equal to  $\sigma_{z_{\text{phot}}}$ . We also determine  $N(z)$ , which is the galaxy distribution

<sup>6</sup> Nevertheless, [Cucciati et al. \(2014\)](#) demonstrate that the major source of uncertainties in the procedure is not the presence of gaps but the incompleteness of the spectroscopic sample (i.e. the  $\sim 35\%$  sampling rate). Besides that, we emphasise that the  $z_{\text{phot}}$  sample is crucial for avoiding any environmental bias caused by the slit assignment. In fact, the VIMOS sampling rate could be slightly lower in crowded regions, because of the minimum distance required between two nearby slits.

along the line of sight of the target. To do that, we take all the objects of the spectroscopic sample lying inside a cylinder with  $7.1 h_{70}^{-1}$  Mpc comoving radius<sup>7</sup> and half-depth of  $\pm 3\sigma_{z_{\text{phot}}}$ ; the cylinder is centred on the coordinates (RA, Dec,  $z_{\text{phot}}$ ) of the considered galaxy. The desired  $N(z)$  distribution is obtained from those objects, using their  $z_{\text{spec}}$  values (without errors) in bins of  $\Delta z = 0.003$ . Then, we multiply the PDF of  $z_{\text{phot}}$  by  $N(z)$  and renormalise the resulting function. In this way we obtain a new PDF whose peaks represent the desired set of  $z_{\text{peak}}$  values. Their respective  $w_{\text{peak}}$  are provided according to the relative height of each peak (the sum of them being equal to one).

We therefore computed the local density  $\rho$  for each of the 33 952 galaxies of the VIPERS (flux-limited) catalogue from  $z = 0.51$  to  $0.9$ . Given the galaxy coordinates  $r_g = (\text{RA}_g, \text{Dec}_g)$  and redshift  $z_g$ ,  $\rho(r_g, R_{5\text{NN}})$  is equal to the number of tracers inside a cylindrical filter centred on  $r_g$ ; the cylinder has a half-depth of  $\Delta v = \pm 1000 \text{ km s}^{-1}$  and radius equal to  $R_{5\text{NN}}$ , i.e. the projected distance of the fifth closest tracer (or fifth nearest neighbour, hereafter 5NN). It should be noticed that such an estimate depends on the absolute magnitude of the tracers. By using fainter tracers (e.g., limited at  $M_B < -19.5 - z$ ), the object identified as 5NN would change and  $R_{5\text{NN}}$  would be generally smaller. However, although the absolute value of  $\delta$  varies as a function of tracer luminosity, we are interested in a relative classification that divides galaxies in under- and overdensities (see Sect. 3.1). Therefore, a different cut in  $M_B$  would not alter our findings because we verified that the galaxy ranking in density contrast would, on average, be preserved. On the other hand, fainter tracers would be incomplete already at lower redshifts. (For example, by assuming  $M_B < -19.5 - z$ , we would restrict our analysis at  $z < 0.7$ .)

The density contrast is defined on scales that differ from one galaxy to another. Namely, in our reconstruction  $R_{5\text{NN}}$  ranges from  $\sim 2.8$  to  $8.6 h_{70}^{-1}$  Mpc while moving from the densest regions towards galaxies with the lowest  $\rho$ . Probing a non-uniform scale does not impair our analysis, because we are interested in a relative classification of different environments (see Sect. 3.1). The 5NN estimator leads to the desired ranking. We adopt the 5NN because it is an adaptive estimator that efficiently samples a broad range of densities. Using, instead, a fixed radius of  $\sim 3 h_{70}^{-1}$  Mpc (i.e. comparable to the 5NN distance in the highest densities), the reconstruction would have been highly affected by shot noise in the VIPERS regions with medium-to-low density. In those regions, the number of tracers inside a filter with a small fixed aperture is very low: considering, for example, that at  $z \approx 0.7$  the mean surface density of tracers is about 85 objects per  $\text{deg}^2$ , only three tracers are expected on average within a cylinder having  $R \approx 3 h_{70}^{-1}$  Mpc.

The use of cylinders, instead of, say, spherical filters, minimises the impact of redshift-space distortions (Cooper et al. 2005). The depth along the line of sight ( $2000 \text{ km s}^{-1}$ ) is optimal not only for spectroscopic redshifts, but also for photometric ones after multiplying their PDF by  $N(z)$  as described above. The reconstruction of the density field through the procedure described here is extensively tested in Cucciati et al. (2014), but using spherical filters with  $R_{\text{fixed}} = 7.1$  and  $11.4 h_{70}^{-1}$  Mpc (5 and 8 Mpc if  $H_0 = 100 \text{ km s}^{-1} \text{ Mpc}^{-1}$ ). We verified that the outcomes do not change when replacing spheres with cylinders (Cucciati et al. in prep.). For a detailed comparison among different filters (spheres or cylinders, fixed or adaptive apertures, etc.), we refer to Kovač et al. (2010a) and Muldrew et al. (2012).

The local density contrast of a given galaxy is

$$\delta(r_g, z_g, R_{5\text{NN}}) = \frac{\rho(r_g, z_g, R_{5\text{NN}}) - \bar{\rho}(z_g)}{\bar{\rho}(z_g)}, \quad (1)$$

where we estimate  $\bar{\rho}(z_g)$  as a function of redshift by smoothing the spectroscopic distribution  $N(z)$  with the  $V_{\text{max}}$  statistical approach in a similar way to Kovač et al. (2010a). For galaxies near the survey edges, we correct  $\delta$  as in Cucciati et al. (2006), i.e. by rescaling the measured density by the fraction of the cylinder volume within the survey borders. We notice, however, that the scatter in the density field reconstruction is mainly due to the survey strategy (e.g. the sampling rate). The impact of border effects is much less and becomes significant only when most of the cylinder volume ( $> 50\%$ ) is outside the survey area. When this happens, we prefer to discard the object from the sample. We also remove galaxies for which the cylinder is inside the survey borders, but fewer than 60% are included in the spectroscopically observed volume (e.g. when more than 40% of it falls in gaps or in a missing VIMOS quadrant). In that case the density contrast should rely mostly on photometric neighbours, and our estimate would be less accurate. With these two constraints, we excluded about 9% of the objects (almost all located on the edges of the survey).

### 3. Environment and galaxy type classification

A fundamental step in this work is to identify the galaxies residing in two opposite environments, regions of low density (LD) and high density (HD). Broadly speaking, the former ones are regions without a pervasive presence of cosmic structure, whereas the latter are associated with the highest peaks of the matter distribution. Ideally, one would like to link these definitions to the total matter density. However, since the dark matter component is not directly observed, any classification has to rely on some proxy of the overall density field. Our classification relies on the galaxy density contrast evaluated in Sect. 2.4. In addition to this, we divide galaxies by type, to work in each environment with active and passive objects separately.

#### 3.1. Galaxy environments

In our analysis, we distinguish LD from HD environments by means of the local density contrast. We include in the LD (HD) sample galaxies that have a density contrast smaller (larger) than a certain value of  $\delta$ . These thresholds can be fixed according to some physical prescription (e.g. to match detections of galaxy groups or clusters, as in Kovač et al. 2010a) or be determined in a relative way, such as by considering the extreme tails of the  $1 + \delta$  distribution. Following the latter approach, Bolzonella et al. (2010, zCOSMOS 10 k sample) assume, as reference for low and high densities, the 25th and 75th percentiles (i.e., first and third quartiles) of the  $1 + \delta$  distribution, respectively. The authors computed the distribution in each of their redshift bins, independently; however, we notice that the thresholds they estimate in bins between  $z = 1$  and  $0.5$  are almost constant (see also Peng et al. 2010, Fig. 9).

Similar to Bolzonella et al. (2010), we computed the distribution of  $1 + \delta$  (distinctly in W1 and W4) within three redshift bins:  $0.51 < z \leq 0.65$ ,  $0.65 < z \leq 0.8$ ,  $0.8 < z \leq 0.9$ . We chose this partition to probe a volume that is sufficiently large in each bin ( $\geq 7 \times 10^6 h_{70}^{-3} \text{ Mpc}^3$ ). Moreover, the resulting median redshifts ( $\langle z \rangle$ , see Table 1) correspond to nearly equally spaced

<sup>7</sup> This value corresponds to a radius equal to 5 Mpc, if one assumes  $H_0 = 100 \text{ km s}^{-1} \text{ Mpc}^{-1}$  (as in Cucciati et al. 2014).

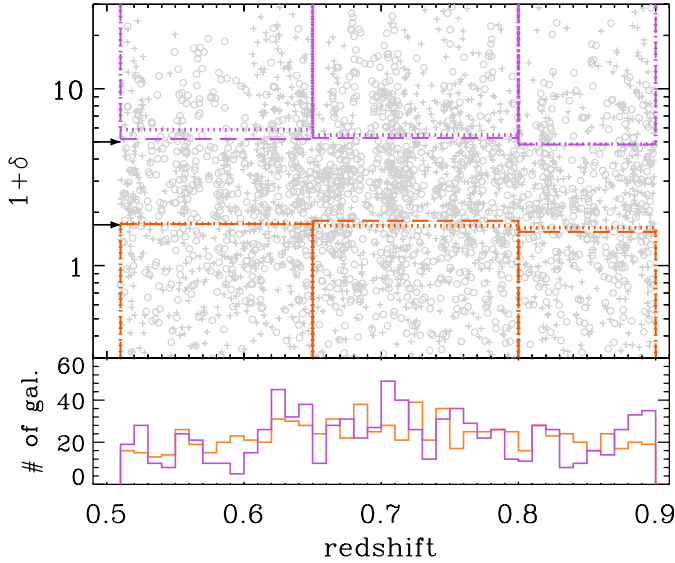


**Fig. 1.** *Upper panel:* galaxy density contrast of a mass-limited sample having  $\log(M/M_{\odot}) > 10.86$ . Galaxies from the W1 field are marked with plus signs, from W4 with open circles. For each redshift bin, galaxies below the 25th (above the 75th) percentile of the  $1 + \delta$  distribution are enclosed by orange (violet) rectangles (dotted lines for W1, dashed lines for W4). The two thresholds that define LD and HD, as discussed in Sect. 3.1, are indicated by an arrow on the left side of the plot. *Lower panel:* combining the two fields together, histograms represent the redshift distribution of the LD and HD sub-sample in orange and violet, respectively.

time steps (0.6–0.7 Gyr). We adopt the same redshift bins to estimate the mass functions in Sect. 4. Here we take only galaxies with  $\log(M/M_{\odot}) > 10.86$  into account to work with a complete sample in all the  $z$ -bins. Indeed, such a value corresponds to the stellar mass limit of the passive population at  $z \approx 0.9$  (see Sect. 4.1 and Table 1). The resulting 25th and 75th percentiles ( $\delta_{LD}$  and  $\delta_{HD}$ ) vary amongst the three  $z$ -bins and the two fields by less than  $\sim 20\%$ , namely  $\delta_{LD}$  assumes values between 0.55 and 0.79, while  $3.84 < \delta_{HD} < 5.87$ . These changes do not represent a monotonous increase as a function of redshift, but rather random variations between one  $z$ -bin and another and between one field and the other (see Fig. 1).

In Appendix A we confirm, by means of cosmological simulations, that the small fluctuations of the percentile thresholds do not reflect an evolution in  $z$ . In fact, they are mainly due to sample variance and do not reflect the growth of structure over cosmic time. Moreover, we verified that there is no bias introduced by the VIPERS selection effect. Therefore, we can safely use constant thresholds to classify LD and HD environments in VIPERS: we consider galaxies with  $1 + \delta < 1.7$  as belonging to LD, and galaxies with  $1 + \delta > 5$  to HD. These limits, applied from  $z = 0.9$  to 0.51, are the mean of the 25th and 75th percentiles computed above (see Fig. 1). Despite the name we chose for sake of clarity, we note that the HD regions in VIPERS actually have intermediate densities in absolute terms. Very concentrated structures, such as massive galaxy clusters, typically have  $1 + \delta \approx 15\text{--}20$  (Kovač et al. 2010a) and should approximately match the upper 5% of environmental density. However, the HD environment we defined, although on average less extreme, is certainly interesting to study, since it has evolved more recently than typical clusters (Smith et al. 2005; Fritz et al. 2005).

As stated above, with the 5NN we tend to probe  $3\text{--}8 h_{70}^{-1}$  Mpc. As a result, if a certain environmental mechanism

were efficient on a smaller scale, its trace could be “diluted”, or even vanish, in our analysis. However, this is not the case, as we show in the following. Environmental dependencies on large scales have already been measured as in Cucciati et al. (2006) (see also Bassett et al. 2013; Hearin et al. 2015). These findings can be due to physical mechanisms operating at distances larger than the halo virial radius (e.g. Lu et al. 2012). Another possibility is that a connection between large-scale environment and halo properties preserves the small-scale signal even when working with lower resolutions. Supporting the latter argument, Haas et al. (2012) demonstrate that estimators based on a number of neighbours  $2 \leq N \leq 10$  correlate equally well with host halo mass.

Further details about the estimate of the density field are given in Appendix A. Among the tests described there, we also evaluate the purity and completeness of our LD and HD samples. By working on mock galaxy catalogues, we show that our method is not hindered by the VIPERS selection function: more than 70% of LD/HD galaxies are expected to be assigned to the correct environment, while a small tail of objects ( $< 8\%$ ) end up in the opposite one as interlopers.

### 3.2. Classification of galaxy types

To separate active and passive galaxies, we apply the method described in Arnouts et al. (2013), based on the  $(NUV - r)$  vs.  $(r - K)$  diagram (NUVrK in the following). With this method, recent star formation on a scale of  $10^6\text{--}10^8$  yr is traced by the  $(NUV - r)$  colour (Salim et al. 2005), while  $(r - K)$  is sensitive to the inter-stellar medium (ISM) absorption. The absolute magnitudes used here have been estimated as explained in Sect. 2.3, through the filters NUV,  $r$ , and  $Ks$  of GALEX, MegaCam, and WIRCam, respectively. It should be noticed that our redshift range ( $0.51 < z \leq 0.9$ ) is fully within the interval  $0.2 < z < 1.3$  used by Arnouts et al. in their analysis. Their diagram is similar to the  $(U - V)$  vs.  $(V - J)$  plane proposed by Williams et al. (2009), but by sampling more extreme wavelengths, it results in a sharper separation between quiescent and star-forming galaxies (cf. also Ilbert et al. 2013). Moreover, the position of a galaxy in the NUVrK plane correlates well with its infrared excess (IRX, i.e. the  $L_{IR}/L_{NUV}$  ratio) and specific SFR ( $sSFR \equiv SFR/M_{\odot}$ , at least when  $\log(M/M_{\odot}) \geq 9.3$  (for further details, see Arnouts et al. 2013). It should also be emphasised that with classification methods based on a single-colour bimodality, the passive sample is partially contaminated by star-forming galaxies reddened by dust, as shown by Moresco et al. (2013), among others. With the NUVrK, the simultaneous use of two colours disentangles those different populations.

As illustrated in Fig. 2 (solid line), we regard a galaxy as passive when

$$\begin{aligned} (NUV - r) &> 3.75 \quad \text{and} \\ (NUV - r) &> 1.37(r - K) + 3.2 \quad \text{and} \\ (r - K) &< 1.3. \end{aligned} \quad (2)$$

Active galaxies are located in the complementary region of the diagram (i.e. below the solid line in Fig. 2).

With respect to the definition of Arnouts et al. (2013), we added a further cut, namely  $(r - K) < 1.3$ . In this way we take the geometrical effect they observe into account after including the dust prescription of Chevallard et al. (2013) in their analysis. According to that study, the reddest  $(r - K)$  colours can only be reached by edge-on disc galaxies with a flat attenuation curve. We also verified through a set of BC03 templates that passive



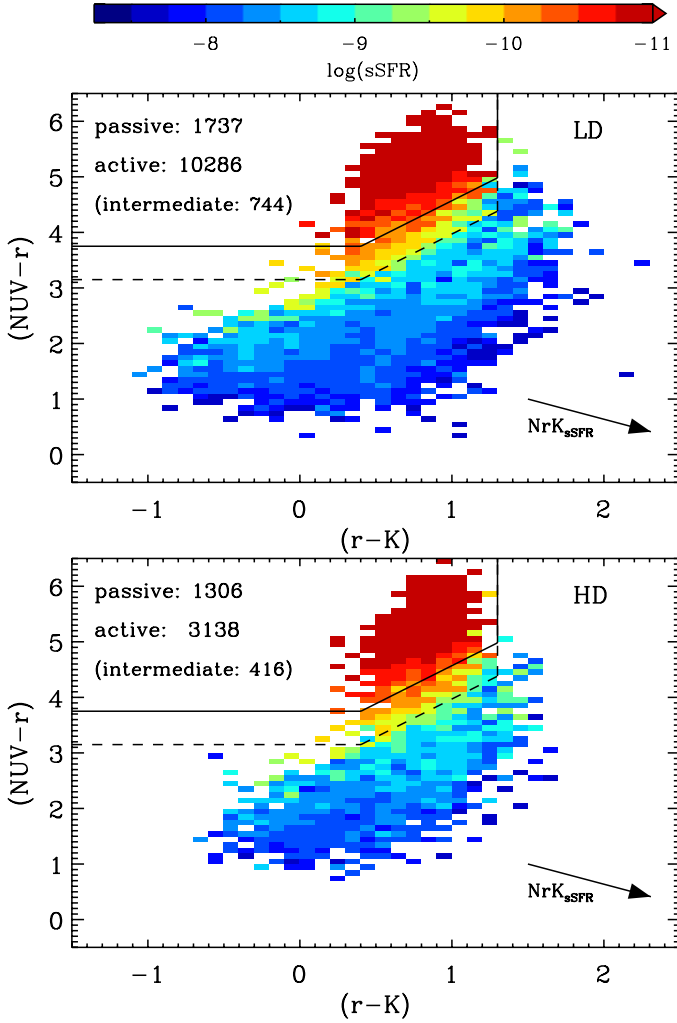


**Fig. 2.** NUVrK diagram of the VIPERS galaxies between  $z = 0.51$  and  $0.9$ , in the LD environment (top panel) and in HD (bottom panel). According to our classification, passive galaxies lie above the solid line (defined in Eq. (2)), while the dashed line (Eq. (3)) divides galaxies with intense star formation (bottom part of the diagram) from those having low sSFR (see text). In the rest of the paper, the two classes are treated as a whole sample of active objects. Their number (and the number of passive galaxies) in each environment is shown in the top-left corner of the plots. Each colour-coded pixel represents the median sSFR of the galaxies inside it, estimated by means of SED fitting. Arnouts et al. (2013) find that in this diagram the sSFR increases because moving along the direction  $[(r - K), (NUV - r)] = [(r - K)_0 + \sin(54^\circ), (NUV - r)_0 - \cos(54^\circ)]$ , identified by the bottom-right vector  $NrK_{sSFR}$  (note that the different scale in  $x$ - and  $y$ -axis warps the angles).

galaxies ( $\text{age}/\tau > 4$ ) have  $(r - K) < 1.15$ . Considering the typical uncertainties in magnitude estimates, this result justifies the third condition in Eq. (2). With a similar argument, Whitaker et al. (2011) modify the passive locus of Williams et al. (2009) diagram.

In the NUVrK, sSFR increases as galaxies move in a preferred direction, identified in Fig. 2 by the vector  $NrK_{sSFR}$ . Therefore, lines orthogonal to that direction work as a cut in sSFR: for instance, the diagonal boundary we defined for the passive locus roughly corresponds to  $\text{sSFR} < 10^{-11} \text{ yr}^{-1}$ . We prefer to use NUVrK instead of selecting directly through the sSFR distribution, since the SED fitting estimates of SFR

are generally less reliable than colours (Conroy et al. 2009), especially when far-IR data are not available. Nevertheless, it is worth noticing that the sSFR values we obtained from *Hypermass* are on average in good agreement with the NUVrK classification, providing an additional confirmation of its robustness (see Fig. 2). Among the galaxies we have classified as NUVrK-passive, about 95% have a (SED fitting derived) sSFR lower than  $10^{-11} \text{ yr}^{-1}$  (which is the typical cut used e.g. in Pozzetti et al. 2010).

We also tested another boundary in the colour-colour space (the dashed line in Fig. 2), namely

$$\begin{aligned} (NUV - r) &> 3.15 \quad \text{and} \\ (NUV - r) &> 1.37(r - K) + 2.6 \quad \text{and} \\ (r - K) &< 1.3. \end{aligned} \quad (3)$$

In this way we can delimit a region in the NUVrK plane likely corresponding to the “green valley”: galaxies in between Equations (2) and (3) are probably shutting off their star formation, having  $\text{sSFR} \approx 10^{-10} \text{ yr}^{-1}$  according to their SED fitting estimates (Fig. 2; but see also Arnouts et al. 2013). We include these galaxies in the active sample, although they are expected to be in transition towards the passive locus. We verify that removing them from the active sample does not modify our conclusions. The typical features of these “intermediate” galaxies will be explored in a future work.

#### 4. Stellar mass functions in different environments

We now derive the stellar mass function of VIPERS galaxies within the environments described in Sect. 3.1, also separating active and passive subsamples. The chosen redshift bins are those already adopted there (also reported in Table 1). We describe our results and compare them to what has been found by previous surveys.

##### 4.1. Methods

First, we determine the threshold  $M_{\text{lim}}$  above which our data can be considered complete in stellar mass. As explained below,  $M_{\text{lim}}$  depends on the flux limit of VIPERS ( $i_{\text{lim}}$ ), redshift, and galaxy type. Such a limit excludes stellar mass bins with large numbers of undetected objects.

The estimate of  $M_{\text{lim}}$  is complicated by the wide range of  $M/L$ . To estimate such a limit, we apply the technique of Pozzetti et al. (2010), which takes typical  $M/L$  of the faintest observed galaxies into account (see also the discussion in D13, Sect. 3.1). We keep the active sample separated from the passive one, since  $M/L$  depends on galaxy type. For each population we select the 20% faintest objects inside each redshift bin. We rescale their stellar masses at the limiting magnitude:  $\log(M(i=i_{\text{lim}})/M_\odot) \equiv \log(M/M_\odot) + 0.4(i - i_{\text{lim}})$ . For the active and passive samples, we define  $M_{\text{lim}}^{\text{act}}$  and  $M_{\text{lim}}^{\text{pass}}$  to be equal to the 98th and 90th percentiles of the corresponding  $M(i=i_{\text{lim}})$  distributions, respectively. We choose a higher percentile level for active galaxies to take the larger scatter they have in  $M/L$  into account. Results are reported in Table 1. The increase in the limiting mass towards higher redshifts is due to dimming, while  $M_{\text{lim}}^{\text{act}}$  is always lower than  $M_{\text{lim}}^{\text{pass}}$  because passive SEDs have on average a higher  $M/L$ . For the total GSMF, we use  $M_{\text{lim}}^{\text{pass}}$  as a conservative threshold; a direct estimate by applying the technique of Pozzetti et al. (2010) to the whole sample would result in lower values by about 0.2–0.3 dex, because of the mixing of galaxy types (cf. D13; Moustakas et al. 2013).



**Table 1.** Stellar mass completeness: thresholds for active and passive galaxies in the redshift bins adopted in this work.

Redshift range	$\langle z \rangle$	$\log(\mathcal{M}_{\text{lim}}^{\text{act}}/\mathcal{M}_{\odot})$	$\log(\mathcal{M}_{\text{lim}}^{\text{pass}}/\mathcal{M}_{\odot})$
$0.51 < z \leq 0.65$	0.60	10.18	10.39
$0.65 < z \leq 0.8$	0.72	10.47	10.65
$0.8 < z \leq 0.9$	0.84	10.66	10.86

**Notes.** These limits are valid in both LD and HD regions;  $\mathcal{M}_{\text{lim}}^{\text{pass}}$  is also used for the whole galaxy sample. In addition, the median redshift of each bin is reported in the second column.

We then estimate the stellar mass functions by means of two methods, namely the  $1/V_{\text{max}}$  method (Schmidt 1968) and the one devised by Sandage et al. (1979, hereafter STY). The former is non-parametric, whereas the latter assumes the GSMF to be modelled by the Schechter (1976) function

$$\Phi(\mathcal{M})d\mathcal{M} = \Phi_{\star} \left( \frac{\mathcal{M}}{\mathcal{M}_{\star}} \right)^{\alpha} \exp \left( -\frac{\mathcal{M}}{\mathcal{M}_{\star}} \right) \frac{d\mathcal{M}}{\mathcal{M}_{\star}}. \quad (4)$$

Both of them are implemented in the software package ALF (Ilbert et al. 2005).

The  $1/V_{\text{max}}$  method gives the comoving galaxy density in a certain stellar mass bin (e.g. between  $\mathcal{M}$  and  $\mathcal{M} + d\mathcal{M}$ ):

$$\Phi(\mathcal{M})d\mathcal{M} = \sum_{j=1}^N \frac{w_j}{V_{\text{max},j}}, \quad (5)$$

where  $V_{\text{max}}$  is the comoving volumes in which a galaxy (out of the  $N$  detected in the given bin) would be observable, and  $w$  is the statistical weight described in Sect. 2.2. Usually, to measure  $V_{\text{max}}$  one needs to know the sky coverage of the survey, and the minimum and maximum redshifts at which the object drops out of the magnitude range of detection. However, considering the whole surveyed area is not formally correct when dealing with HD/LD galaxies – as well as galaxies in clusters or groups – because those objects have no chance (by definition) of being observed outside their environment. In other words, we need to reconstruct the comoving volumes occupied by the HD/LD regions and take them into account, instead of the total VIPERS volume, to estimate the  $V_{\text{max}}$  values. This new approach is described in detail in Appendix B. It allows us to properly normalise the stellar mass functions in Fig. 3. In the same Appendix we also describe how we estimated the uncertainty due to cosmic variance by means of galaxy mocks. We include this uncertainty in the error budget of the total GSMFs, along with Poisson noise, while for the active and passive samples, we only compute errors assuming Poisson statistics. In plotting each GSMF, the  $1/V_{\text{max}}$  points are located at the median stellar mass of their bin. We evaluate the error on this position, i.e. the error bar on the  $x$ -axis, by considering 100 simulated Monte Carlo samples in which the uncertainty of  $\log(\mathcal{M}/\mathcal{M}_{\odot})$  is randomly assigned from a Gaussian that is 0.2 dex large. After binning those samples, the median stellar mass within each bin shows a variance that is on average smaller than 0.05 dex, which is fully negligible in the treatment.

The STY method determines the parameters  $\alpha$  and  $\mathcal{M}_{\star}$  of Eq. (4) through a maximum-likelihood approach. The associated uncertainties come from the confidence ellipsoid at  $1\sigma$  level. In the highest redshift bin, i.e.  $0.8 < z < 0.9$ , we are limited to  $\log \mathcal{M}/\mathcal{M}_{\odot} \gtrsim 10.7$ , so we prefer to keep  $\alpha$  fixed to the value found in the previous  $z$ -bin. The third parameter ( $\Phi_{\star}$ ) is computed independently, to recover the galaxy number density after

integrating the Schechter function (see Efstathiou et al. 1988; Ilbert et al. 2005). Also in this case we consider the comoving volumes occupied by the two environments (Appendix B).

The STY estimates are listed in Table 2, along with their uncertainties. Complementary to the  $1/V_{\text{max}}$  estimator in many aspects, this method is unbiased with respect to density inhomogeneities (see Efstathiou et al. 1988). We verified that the  $1/V_{\text{max}}$  outcomes are reliable by comparing its outcomes not only with the STY but also with another non-parametric estimator (i.e. the stepwise maximum-likelihood method of Efstathiou et al. 1988). These multiple estimates strengthen our results, since the different methods turn out to be in good agreement (Fig. 4). In particular, this fact validates the completeness limits we have chosen because the estimators would diverge at  $\mathcal{M} > \mathcal{M}_{\text{lim}}$  if some galaxy population were missing (see Ilbert et al. 2004).

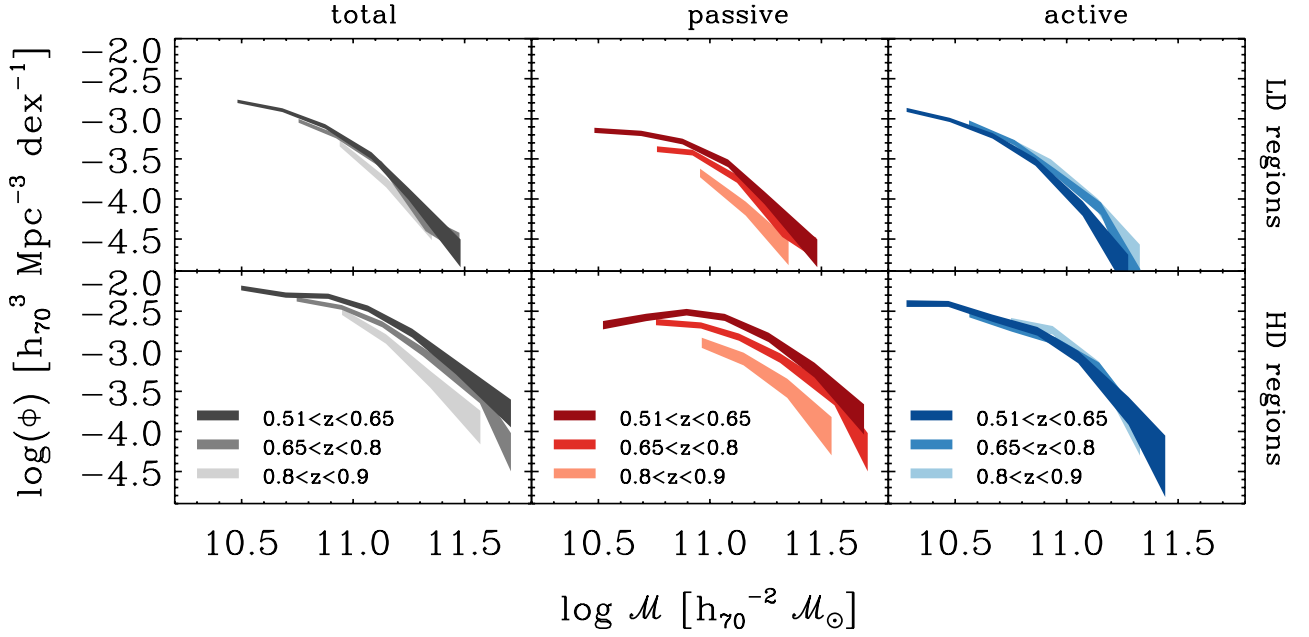
#### 4.2. Results

The GSMFs computed in this section are shown in Figs. 3 and 4. In the former, to show their evolution, we superimpose the mass functions at different redshifts, namely  $0.51 < z \leq 0.65$ ,  $0.65 < z \leq 0.8$ , and  $0.8 < z \leq 0.9$  (median redshift  $\bar{z} \sim 0.6, 0.72, 0.84$ ). On the other hand, in Fig. 4, we renormalise the GSMFs in such a way that their number density is equal to unity when we integrate the GSMF at  $\mathcal{M} > \mathcal{M}_{\text{lim}}$ . With this kind of rescaling, we can directly compare the shape that the GSMF has in the two environments. In both figures, the mass functions of different galaxy types (total, passive, and active samples) are plotted in distinct columns.

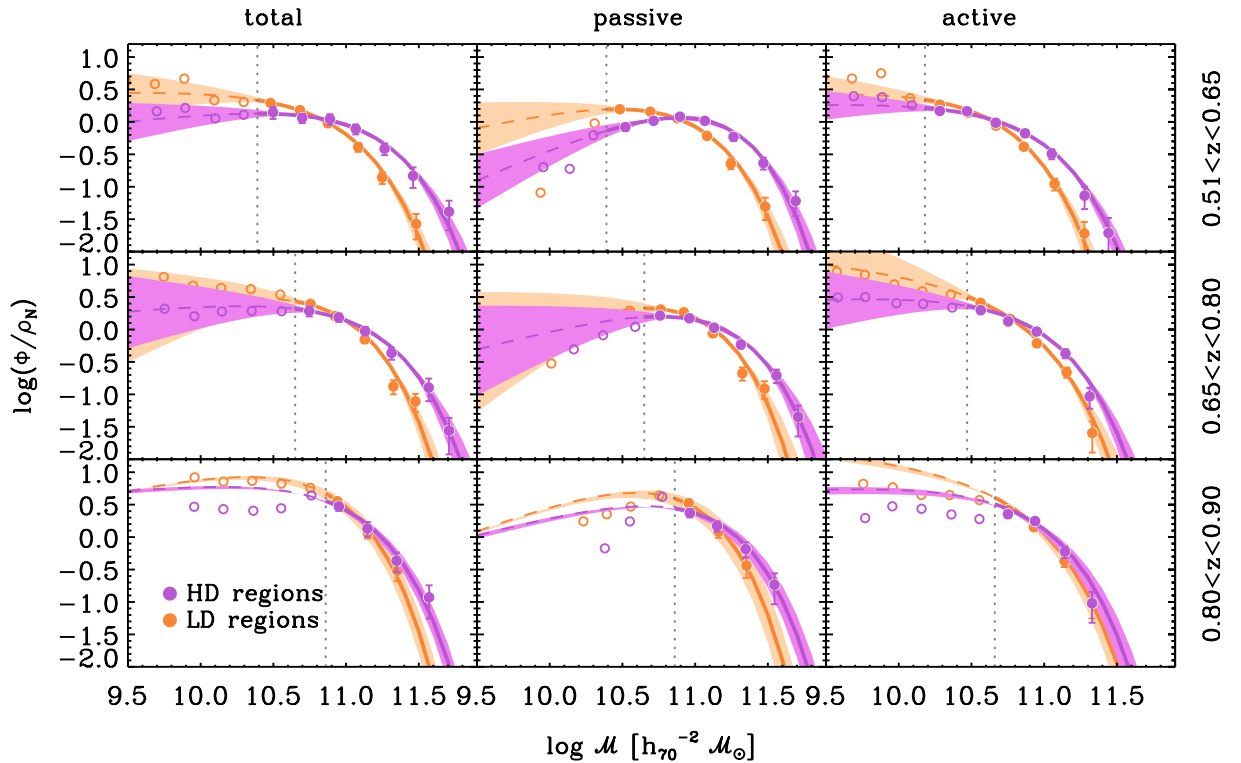
Our results are particularly intriguing in the high-mass regime, where VIPERS benefits from its large number statistics. Figure 3 shows a different growth of stellar mass in LD and HD environments. Regarding the total galaxy sample, there is a mild increase in the HD high-mass tail over cosmic time (bottom-left panel), an increase that is observed neither in LD (top-left panel) nor in the GSMF of the whole VIPERS volume (D13). This trend seems to be due to the passive population (central panels) and is investigated in Sect. 5.

Also looking at the shape of the GSMFs, there is a remarkable difference between LD and HD galaxies (Fig. 4). At  $z \leq 0.8$ , a large number of massive galaxies inhabit the densest regions, resulting in a higher exponential tail of the HD mass function with respect to the LD environment. At higher redshifts this difference becomes less evident. Quantitatively, the difference is described well by the Schechter parameter  $\mathcal{M}_{\star}$ , which is larger in the HD regions (see the likelihood contours for  $\alpha$  and  $\mathcal{M}_{\star}$  shown in Fig. 5). For the total sample, in the first and second redshift bins,  $\Delta\mathcal{M}_{\star} \equiv \log(\mathcal{M}_{\star,\text{HD}}/\mathcal{M}_{\star,\text{LD}}) = 0.24 \pm 0.12$  and  $0.27 \pm 0.15$  dex, respectively. A similar deviation appears at  $0.8 < z \leq 0.9$  ( $\Delta\mathcal{M}_{\star} = 0.21 \pm 0.11$  dex), although in that case the formal  $\mathcal{M}_{\star}$  uncertainty has been reduced by keeping  $\alpha$  fixed in the fit. The behaviour seen for the whole sample is also a signature of the GSMFs divided by galaxy types (Fig. 4, middle and right panels).

At intermediate masses, our analysis becomes less stringent. Given the completeness limit of VIPERS, it is difficult to constrain the power-law slope of the GSMF. We find that  $\alpha_{\text{HD}}$  and  $\alpha_{\text{LD}}$  are compatible within the errors, with the exception of the passive sample at  $0.51 < z \leq 0.65$ , for which the stellar mass function is steeper in the LD regions.



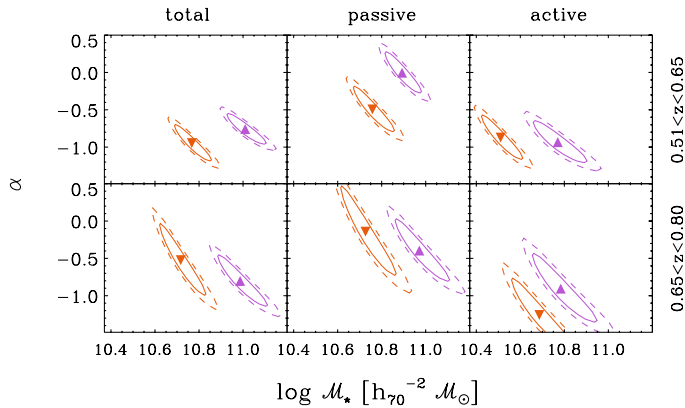
**Fig. 3.** Evolution of the GSMF in the different VIPERS environments. Total, passive, and active samples are in black, red, and blue colours, respectively. Each shaded area is obtained from the  $1/V_{\max}$  estimates by adding the corresponding Poissonian uncertainty (see Sect. 4.1 and Appendix B for details); only estimates above the stellar mass completeness limit are considered.



**Fig. 4.** Stellar mass functions of galaxies at low density (orange symbols) and high density (violet symbols) in three different redshift bins, namely  $0.51 < z \leq 0.65$ ,  $0.65 < z \leq 0.8$ , and  $0.8 < z \leq 0.9$ . *Right panels* show the GSMFs of active galaxies, while *central panels* refer to passive ones. The GSMFs of the whole sample in the same  $z$ -bins are shown on the *left*. In each plot, filled (open) circles represent the  $1/V_{\max}$  points above (below) the completeness mass  $M_{\text{lim}}$  (vertical dot line), with error bars (shown only above  $M_{\text{lim}}$ ) that account for Poisson uncertainty. In the total GSMFs, the uncertainty due to cosmic variance is also added in the error bars. (In some cases, the error bar is smaller than the size of the points.) Solid lines represent the Schechter functions estimated through the STY method, with the  $1\sigma$  uncertainty highlighted by a shaded area. With this estimator, all the Schechter parameters are free, except at  $0.8 < z \leq 0.9$ , where  $\alpha$  is fixed to the value found in the previous  $z$ -bin (see Table 2). To compare the shape of mass functions in LD and HD, we renormalise them in such a way that their number density ( $\rho_N$ ) is equal to unity when we integrate the GSMF at  $M > M_{\text{lim}}$ .

**Table 2.** GSMF in low- and high-density regions: Schechter parameters resulting from the STY method, when applied to different galaxy populations at different redshifts.

Galaxy sample	$\alpha$	$\log M_*$ [ $h_{70}^{-2} M_\odot$ ]	$\Phi_*$ [ $10^{-3} h_{70}^3 \text{Mpc}^{-3}$ ]	$\alpha$	$\log M_*$ [ $h_{70}^{-2} M_\odot$ ]	$\Phi_*$ [ $10^{-3} h_{70}^3 \text{Mpc}^{-3}$ ]
		low density		high density		
0.51 < $z$ < 0.65						
Total	$-0.95^{+0.16}_{-0.16}$	$10.77^{+0.06}_{-0.05}$	$1.27^{+0.17}_{-0.19}$	$-0.76^{+0.14}_{-0.13}$	$11.01^{+0.06}_{-0.06}$	$4.60^{+0.59}_{-0.63}$
Passive	$-0.49^{+0.20}_{-0.20}$	$10.76^{+0.06}_{-0.06}$	$0.73^{+0.06}_{-0.08}$	$-0.00^{+0.18}_{-0.18}$	$10.89^{+0.06}_{-0.05}$	$3.51^{+0.16}_{-0.16}$
Active	$-0.87^{+0.20}_{-0.19}$	$10.51^{+0.06}_{-0.06}$	$1.18^{+0.16}_{-0.19}$	$-0.93^{+0.19}_{-0.18}$	$10.77^{+0.08}_{-0.08}$	$2.71^{+0.55}_{-0.57}$
0.65 < $z$ < 0.80						
Total	$-0.52^{+0.32}_{-0.31}$	$10.72^{+0.07}_{-0.06}$	$1.14^{+0.07}_{-0.11}$	$-0.80^{+0.23}_{-0.22}$	$10.99^{+0.08}_{-0.07}$	$3.83^{+0.55}_{-0.69}$
Passive	$-0.14^{+0.40}_{-0.39}$	$10.73^{+0.09}_{-0.08}$	$0.51^{+0.03}_{-0.04}$	$-0.40^{+0.28}_{-0.27}$	$10.97^{+0.09}_{-0.07}$	$2.42^{+0.18}_{-0.32}$
Active	$-1.26^{+0.32}_{-0.31}$	$10.69^{+0.10}_{-0.09}$	$0.79^{+0.20}_{-0.24}$	$-0.91^{+0.31}_{-0.30}$	$10.78^{+0.10}_{-0.09}$	$2.54^{+0.51}_{-0.65}$
0.80 < $z$ < 0.90						
Total	-0.52	$10.64^{+0.05}_{-0.04}$	$1.16^{+0.08}_{-0.08}$	-0.80	$10.85^{+0.05}_{-0.04}$	$4.59^{+0.33}_{-0.33}$
Passive	-0.14	$10.66^{+0.06}_{-0.05}$	$0.36^{+0.04}_{-0.04}$	-0.40	$10.88^{+0.06}_{-0.05}$	$1.76^{+0.18}_{-0.18}$
Active	-1.26	$10.70^{+0.07}_{-0.07}$	$0.85^{+0.05}_{-0.05}$	-0.91	$10.75^{+0.07}_{-0.06}$	$3.35^{+0.25}_{-0.25}$

**Notes.** Before fitting data at  $0.8 < z < 0.9$ ,  $\alpha$  has been fixed to the value of the previous  $z$ -bin.**Fig. 5.** Schechter (1976) parameters (filled symbols) of the GSMFs at redshift  $0.51 < z < 0.65$  and  $0.65 < z < 0.8$ , where  $\alpha$  was left free during the STY fitting (cf. Fig. 4). The solid- and dashed-line contours represent the 68.3 and 90% CL, respectively. Orange lines and downward triangles are the estimates for galaxies in the LD regions, violet lines, and upward triangles are used for the HD ones. Each panel deals with a different sample (total, passive, and active galaxies from left to right). All the values were obtained by using the algorithms contained in the ALF suite (Ilbert et al. 2005).

#### 4.3. Comparison with previous work

The comparison with other authors is not always straightforward, given the different definitions of environment and galaxy types. Besides that, the selection function (and the completeness) also changes from one survey to another. An approach that is very similar to ours is found in Bolzonella et al. (2010). In that paper, low- and high-density galaxies in the zCOSMOS survey ( $0.1 < z < 1.0$ ) are classified by means of the galaxy density contrast (derived from the 5NN, as in our case)<sup>8</sup>. Bolzonella et al. observe the number density of massive galaxies to be higher

in overdense regions, although within the uncertainties of the GSMF estimates. Down to the redshift range not reached by VIPERS ( $0.1 < z < 0.5$ ), they also find an upturn of the high-density GSMF below  $\log M/M_\odot \lesssim 10$ .

In Fig. 6 we compare our GSMFs directly to those of Bolzonella et al. (2010) in a redshift bin that is similar in the two analyses ( $0.5 < z < 0.7$  in their paper,  $0.51 < z < 0.65$  in ours). We find good agreement for both passive and active galaxies<sup>9</sup>. With respect to the latter sample, a better accordance is reached when considering only high-sSFR galaxies, i.e. when we remove the “intermediate” objects that lie between the borders (2) and (3) of the NUVrK diagram. This improvement is probably the result of the high-sSFR subsample being more similar to the late-type galaxies of Bolzonella et al. (2010), which they identify using an empirical set of galaxy templates. We note that also in Bundy et al. (2006) a difference between LD and HD mass function is visible but not significant (Bundy et al. 2006, Fig. 11). With a combination of photometric redshift samples, Mortlock et al. (2014) conducted a study of environmental effects up to  $z \sim 2.5$ . Their analysis suggests that massive galaxies at  $z < 1$  favour denser environments. When they derived the GSMF in this environment, they also observed a flatter low-mass end, in agreement with our findings. In contrast, at  $z > 1$  the GSMFs in low and high densities become very similar.

Other studies, however, find no environmental dependency in the stellar mass function of galaxy clusters (Calvi et al. 2013; Vulcani et al. 2012, 2013; van der Burg et al. 2013). The lack of differences in the field vs. cluster comparison can be due to the various (local) environments embraced in the broad definition of “field” (i.e. a sky region without clusters) that can include single galaxies, pairs, and even galaxy groups. Simulations of McGee et al. (2009) indicate that the majority of cluster members have been accreted through galaxy groups. Other models, such as those used in De Lucia et al. (2012), similarly show that

<sup>8</sup> For the sake of simplicity, we also use our notation (LD and HD) when referring to the low-/high-density galaxies of Bolzonella et al. (2010), which are named D1 and D4 in the original paper.

<sup>9</sup> When considering the next bin of Bolzonella et al., i.e.  $0.7 < z < 1$ , we also found fairly good agreement with our data at  $0.65 < z < 0.9$ . However, we preferred to show the  $z$ -bin where the stellar mass limit is lower.



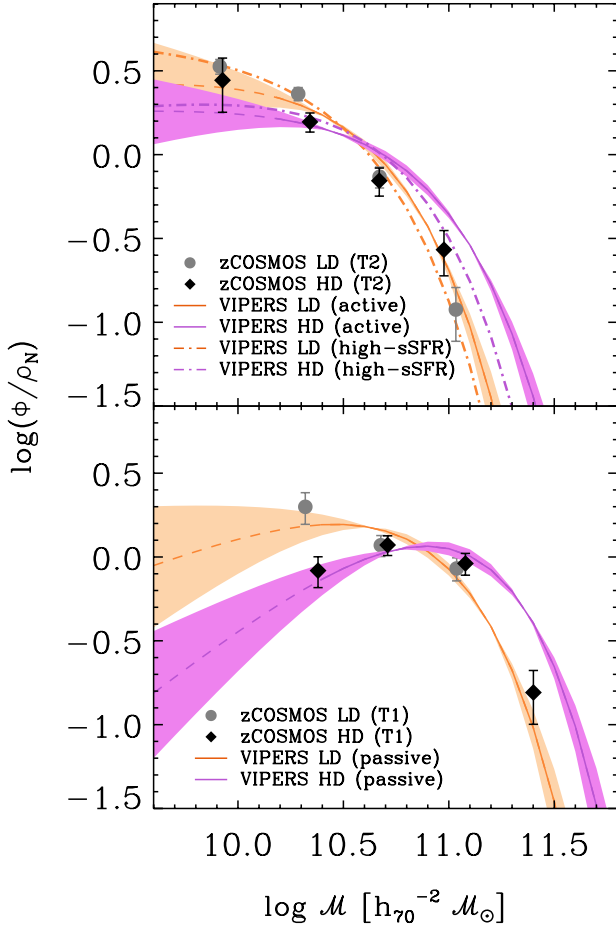


**Fig. 6.** VIPERS (this work) and  $z$ COSMOS (Bolzonella et al. 2010) stellar mass functions of galaxies in LD/HD regions (orange/violet and grey/black colours, see the legend in the top-right corner of each panel). The comparison is restricted to a single redshift bin that is similar in the two surveys ( $0.5 < z < 0.7$  in  $z$ COSMOS,  $0.51 < z < 0.65$  in VIPERS). All the GSMFs are rescaled to have  $\rho_N(M > M_{\text{lim}}) = 1$ , as in Fig. 4. In both panels, solid lines represent the STY estimates for the various galaxy samples, with a shaded area encompassing the  $1\sigma$  uncertainty. (The line is dashed below the stellar mass limit.) Filled circles and diamonds are the  $1/V_{\text{max}}$  determinations of the GSMFs of  $z$ COSMOS (LD and HD, respectively). The *upper panel* includes the stellar mass functions of star-forming galaxies, classified by Bolzonella et al. (2010) according to their photometric types (T2, i.e. late-type galaxies), and by means of the NUVrK diagram in our analysis. With dot-dashed lines we also show the stellar mass function of the VIPERS galaxies having high sSFR (i.e. those remaining after removing the NUVrK-intermediate objects from the active sample). In the *lower panel*, the VIPERS passive sample and the  $z$ COSMOS early-type galaxies (i.e. T1 spectrophotometric types) are considered.

a large number of cluster galaxies belonged to smaller groups before and were ‘pre-processed’ in that environment. Therefore, as galaxy groups also contribute to the stellar mass function in the field, the high-mass end is expected to be similar in the two environments. Indeed, when Calvi et al. (2013) consider only isolated galaxies, they obtain a stellar mass function that differs from the others. The presence of structures in the field can thus be crucial in this kind of analysis.

The (global) environment represented by a galaxy cluster before includes regions with different local conditions. We note that in Vulcani et al. (2012), the local galaxy density also assumes a wide range of values in clusters. The issue is also discussed by Annunziatella et al. (2014), who analysed a cluster

from the CLASH-VLT survey. They find that the stellar mass function of passive galaxies in the core shows a steeper decrease at low masses, in comparison with passive galaxies in the outskirts of the cluster. In addition, we emphasise that VIPERS is better designed than current cluster surveys to probe  $M > M_*$ . For instance, van der Burg et al. (2013) have 12 spectroscopic members in their 10 GCLASS clusters with  $11.2 < \log(M/M_\odot) < 11.6$  and no detection at higher masses; instead, our HD regions contain a few hundred (spectroscopic) galaxies above  $\log(M/M_\odot) = 11.2$ .

To summarise, the comparison illustrates the advancement VIPERS represents with respect to previous surveys like  $z$ COSMOS or DEEP2: we are now able to robustly distinguish the LD and HD mass functions, finding differences that were not statistically significant before. We emphasise that VIPERS also has more statistical power than current cluster surveys for probing the massive end of the GSMF. Besides that, that our results disagree, for instance, with Vulcani et al. (2012) is related to the different definition of environment. On the other hand, the sample used in this paper spans only  $\sim 2.3$  Gyr of the history of the Universe, whereas  $z$ COSMOS and DEEP2 have a wider redshift range. Future spectroscopic surveys will combine high statistics and large cosmic time intervals thanks to the next-generation facilities (especially PFS, the Subaru Prime Focus Spectrograph Takada et al. 2014). They could confirm that the environmental effects on the GSMF at  $z \lesssim 1$  (i.e. the enhancement of the high-mass end and the flattening of the power-law slope) vanish at higher redshifts, as suggested by Mortlock et al. (2014).

We can also compare the VIPERS mass functions with those measured in the local Universe. In particular, Peng et al. (2010, hereafter P10) define the environment of SDSS galaxies as in Bolzonella et al. (2010), i.e. in a way similar to ours. They find that

- i. values of  $\alpha$  and  $M_*$  for active GSMFs are the same in the LD and HD regions;
- ii. in LD, the stellar mass function of passive galaxies has the same  $M_*$  as the active one;
- iii. comparing the passive GSMF in LD and HD regions, the latter have a higher value of  $M_*$ <sup>10</sup>.

Thanks to the large volume of the VIPERS sample and to the high precision of the redshift measurements, we can verify that these findings extend to intermediate redshifts. We emphasise that at  $z > 0$ , the environmental signatures (i)–(iii) have not been confirmed yet: several studies have provided contrasting clues (cf. Bolzonella et al. 2010; Vulcani et al. 2012; Giodini et al. 2012; van der Burg et al. 2013; Annunziatella et al. 2014).

With respect to the passive mass functions, the STY estimator yields higher  $M_*$  values in the regions of higher density, as stated in (iii). We find such a trend in all three redshift bins (see Table 2). This feature, as we discuss in Sect. 5.2, can be associated with dry major mergers, which are more likely to happen in the overdense regions. Turning to the active GSMFs, we observe (i) and (ii) at  $z > 0.65$ . Indeed, the shape of the active GSMF is similar in the two VIPERS environments, since  $\alpha$  and  $M_*$  computed in LD/HD regions are compatible within the errors. (At  $z \sim 0.84$ , we can compare only  $M_*$  because  $\alpha$  is fixed a-priori.) Moreover,  $M_{*,\text{LD}}^{\text{act}}$  is consistent with  $M_{*,\text{LD}}^{\text{pass}}$ . At  $0.51 < z \leq 0.65$ , the features (i) and (ii) are not observed any longer. We argue that the difficulty in clearly assessing (i) and

<sup>10</sup> In P10, the passive GSMFs are fitted with a double Schechter function. Here we refer only to what concerns the primary (most massive) component.

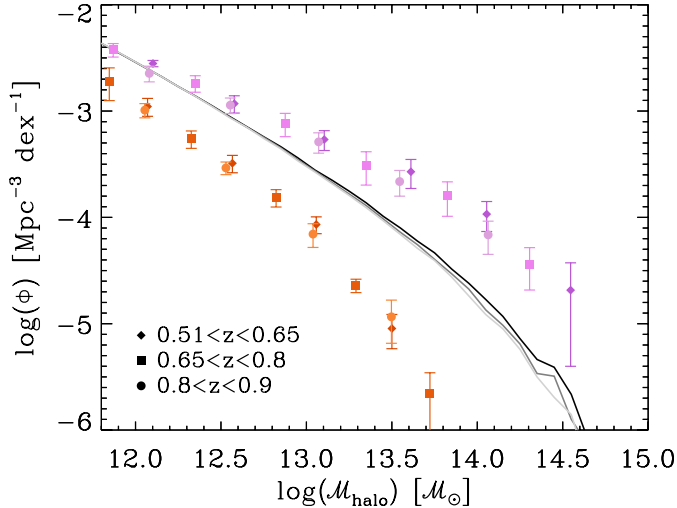


**Fig. 7.** Halo mass function derived from the simulation described in Sect. 5.1, restricted to galaxies in the HD and LD environment (violet and orange symbols, respectively). Different symbols are estimated in the three redshift bins quoted in the bottom-left corner of the plot, with error bars obtained from the variance among the 10 mock catalogues. The mass function of haloes in the entire box ( $714 h_{70}^{-1}$  Mpc side), at snapshots consistent with our redshift bins, is shown as reference with solid lines (darker colour at lower  $z$ ).

(ii) is due to the GSMF parametrisation of the active sample, which here is a single Schechter function (Eq. (4)). Recent work suggests that this is not the optimal choice. For instance, Baldry et al. (2012, GAMA survey) observe an excess of blue galaxies at  $M > 10^{10} M_{\odot}$  with respect to their best (single Schechter) fit, with the magnitude of the deviation depending on the colour adopted to classify. We find that, by adopting a double-Schechter model for the active mass function at  $z \sim 0.6$ , the STY fit produces  $\alpha$  and  $M_{\star}$  that satisfy relations (i) and (ii). However, the uncertainties in this case are larger: given the stellar mass limit of VIPERS, the slope of the secondary component is not well constrained. In the next section we discuss the origin of these GSMF features, which have already been observed in the local Universe and now confirmed at  $0.5 \lesssim z \lesssim 1$

## 5. Discussion

The shape of the passive GSMFs is different in the LD and HD environments, and this difference increases when approaching lower  $z$  (see Fig. 4). This can be the result of an environmental-dependent quenching mechanism, but may also be explained by a different halo mass distribution or a different assembly history for haloes of similar mass but residing in different regions (see discussion in De Lucia et al. 2012). When looking at the halo environment, a similar perspective has been adopted by Hearin et al. (2015) to explain the so-called “galactic conformity” (Weinmann et al. 2006), which is the tendency of satellite galaxies to stay in the same state (star forming or passive) of the central one well beyond the virial radius. Such a sSFR correlation can be linked to the tidal forces that haloes evolving in the same large-scale environment experienced.

### 5.1. Comparison with semi-analytical models

We make use of galaxy simulations to investigate the two environments we defined in more detail. In VIPERS we can exploit a set of ten light cones, built from the Millennium simulation

(Springel et al. 2005). To derive mock catalogues, dark-matter haloes are populated with galaxies by means of the semi-analytic model (SAM) of De Lucia & Blaizot (2007, hereafter DLB07). For each mock galaxy, rest-frame and apparent magnitudes have been estimated in the same filter as used in the real survey, and the same magnitude cut of VIPERS ( $i \leq 22.5$ ) is applied to the simulated catalogue. We add an error to each redshift to emulate observational measurements, either spectroscopic or photometric depending whether the object is chosen to be a VIMOS pseudo-target by the slit positioning algorithm<sup>11</sup>. In Appendices A and B we use these mock catalogues to test our reconstruction of the density field, together with another set realised through the halo occupation distribution (HOD) technique (see de la Torre et al. 2013).

The HOD mock galaxies reproduce VIPERS-PDR1 better: they cover the same area of the real survey and have the colour pre-selection applied. The SAM catalogues were prepared at an earlier stage of the survey, so in each of the ten realisations, the effective area is  $4.5 \text{ deg}^2$ . The decline of  $N(z)$  at  $z \sim 0.5$  due to the VIPERS selection function is reproduced by removing objects randomly, irrespective of their  $(g-r)$  and  $(r-i)$  colours. Nevertheless, the SAM catalogues are better suited to the goal of this section because they contain more physical information. Indeed, the DLB07 model predicts galaxy properties such as stellar mass, SFR, colours at different redshifts, and the apparent magnitudes mentioned above; in contrast, galaxy stellar mass and SFR are not available in the HOD catalogues.

In these Millennium light cones, we identify HD and LD regions through the same method as used with real data (see Sect. 3.1 and Appendix B). In principle, this means that the environmental effects predicted by DLB07 can be straightforwardly compared to those found in VIPERS. However, the LD/HD environments in the simulation may correspond only roughly to the regions delimited in the real survey for several reasons. First, the volume-limited ( $M_B < 20.4 - z$ ) tracers used to estimate  $\delta$  in the simulation may have different number density and clustering. As highlighted in Cucciati et al. (2012), at intermediate redshifts the  $B$ -band luminosity function shows an excess of bright late-type galaxies in the DLB07 model with respect to VVDS data, while early-type galaxies at  $M_B < M_B^{\star}$  are underpredicted. Moreover, we are aware that for the most luminous and massive galaxies, the two-point correlation function of VIPERS is slightly higher than DLB07 on scales  $\gtrsim 7 h_{70}^{-1}$  Mpc (Marulli et al. 2013). This is expected because the  $\sigma_8$  parameter, set by the first-year analysis of the Wilkinson Microwave Anisotropy Probe (WMAP1, Spergel et al. 2003) and adopted in the Millennium simulation, is larger than more recent measurements from WMAP9 and Planck-2015 (Hinshaw et al. 2013; Planck Collaboration XIII 2015). We discuss these differences in Appendix B. Further investigations have been carried out in Cucciati et al. (in prep.). Overall, those tests show that structures (and voids) in the Millennium simulations grow earlier than those in the observed Universe, and the volume occupied by the HD (LD) regions is smaller (larger).

Nevertheless, the under- and overdensities in our light cones still represent two opposite environments that we can contrast, e.g. by looking at their underlying dark matter content. Figure 7 shows the mass distribution of haloes hosting either LD or HD galaxies. In all the redshift bins, the number density of HD

<sup>11</sup> The sampling rate is defined as the ratio between the number of spectroscopic pseudo-targets and the whole mock galaxies sample, in bins of redshift. It is very similar to the TSR of the real survey, while the SSR is 100%. The statistical weighing factor is therefore  $1/\text{TSR}(z)$ .

haloes is higher than the LD ones. The distribution of the former has a flatter slope with a larger number of massive haloes: those with  $M_{\text{halo}} \gtrsim 10^{13.5} M_{\odot}$  are not found in the opposite, low-dense environment. This excess is a clear indication that our environment reconstruction classifies rich galaxy groups and galaxy clusters as HD regions. These results agree with [Fossati et al. \(2015\)](#), who find similar correlations between local galaxy density and halo mass in a thorough study of galaxy environment. We also highlight that the halo number density starts to be higher in HD at masses of  $10^{12}-10^{12.5} M_{\odot}$ . Haloes in this bin should include almost 50% of those galaxies with  $M > 10^{11} M_{\odot}$ , as found by [Popesso et al. \(2015\)](#)<sup>12</sup>.

The difference observed between LD and HD in the high-mass end of the GSMF (Fig. 4) can be interpreted, at least partly, as a reflection of the mass segregation of dark matter. In hierarchical models, massive haloes tend to populate the densest regions (e.g. [Mo & White 1996](#)), and the correlation between halo mass and galaxy stellar mass in turn produces a concentration of massive galaxies in the HD environment (cf. [Abbas & Sheth 2005, 2006](#); [Scodreggio et al. 2009](#); [de la Torre et al. 2010](#)). This gives an idea of how intrinsic properties of the galactic systems are entangled with the classification of their local environment via halo mass, without any solution for the nature vs. nurture dilemma. This picture is consistent with the mass segregation observed by [van der Burg et al. \(2013\)](#) in the GCLASS clusters at  $z \approx 1$ . They normalise their stellar mass function by estimating the total mass (baryons and dark matter) contained within the virial radius of each cluster. On the other hand, their GSMF in the UltraVISTA field is normalised by multiplying its volume by the average matter density of the Universe. After this rescaling, the authors find that the stellar mass function is higher in the clusters than in the field (see [van der Burg et al. 2013, Fig. 8](#)).

We can also derive the stellar mass function of SAM galaxies in LD and HD environments. We already know (see D13) that the DLB07 model overestimates the GSMF low-mass end of the VIPERS field and shows minor tension at higher masses. The same weaknesses are present in more recent SAMs (see e.g. [Fontanot et al. 2009](#); [Cirasuolo et al. 2010](#); [Guo et al. 2011](#); [Maraston et al. 2013](#); [Lu et al. 2014](#)) and also in hydrodynamical simulations. Furthermore, discrepancies arise because of the error sources in the observations (e.g. systematics in stellar mass estimates, see [Marchesini et al. 2009](#); [Bernardi et al. 2013](#)). Most importantly, the LD and HD regions traced in the simulation, although having the same meaning of the real ones, are different e.g. in terms of occupied volume (see discussion above). For this reason we renormalise each GSMF number density to unity (as previously done in Fig. 4).

The shapes of the different GSMFs are compared in Fig. 8. In both environments, at each redshift bin, the shape of the mock GSMF is similar to the observed one after convolving SAM stellar masses with a Gaussian of dispersion 0.2 dex, to reproduce observational uncertainties. The 0.2 dex width has been chosen as an arbitrary value that represents the typical scatter in the SED fitting estimates (see e.g. [Mobasher et al. 2015](#)). We note that a different value (e.g. 0.25 dex, as in [Guo et al. 2011](#)) may result in worse agreement with the data. Aware of this potential bias, we note that it would not remove the difference emerging between HD and LD regions in the simulation. Indeed, the main finding in this section is that mock GSMFs show the same increase of the high-mass end in the densest environment as found in VIPERS.

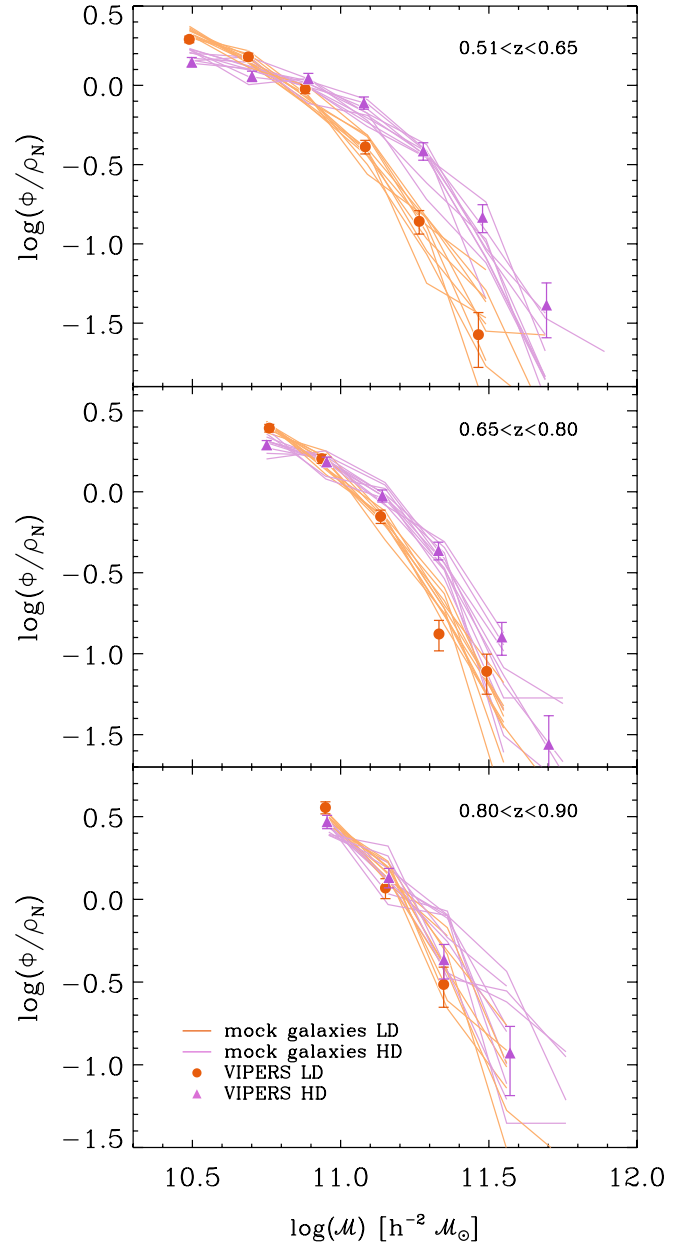


**Fig. 8.** Stellar mass functions of mock galaxies built from the Millennium simulation through the semi-analytical model of [De Lucia & Blaizot \(2007\)](#). The 10 mock realisations correspond to the solid lines (orange and violet for LD and HD regions, respectively), while symbols with error bars show the GSMF of VIPERS in the two environments (the same as Fig. 4). All the mass functions are plotted starting from the completeness limit ( $M_{\text{lim}}$ ) at that redshift. They are obtained by means of the  $1/V_{\text{max}}$  method, rescaled to have the same number density  $\rho_N$  when integrating  $\Phi(M)$  at  $M > M_{\text{lim}}$ .

In addition to this, the model hints at how the low-mass slope changes as a function of environment, at least for the GSMF at  $0.51 < z \leq 0.65$  where the mass range probed is the broadest. Looking at the central galaxies (as defined according to the merger tree), we note that about half of those living in the HD regions are at the centre of a sub-halo already inside a larger structure, while in the LD regions most of them are “isolated” central. Also the number of satellite galaxies, i.e. those embedded in another galaxy halo, increases as a function of  $\delta$ : the HD satellite fraction is a factor  $\sim 2$  higher than the one in LD, reaching about 20% at  $\log(M/M_{\odot}) \sim 10.6$  and going down to zero

<sup>12</sup> We note that both [Fossati et al. \(2015\)](#) and [Popesso et al. \(2015\)](#) use SAMs from the same “family” of DLB07, implemented in a new run of the Millennium simulation.



at  $\log(M/M_\odot) > 11$ . Also, the number of recent mergers (i.e. mergers between two consecutive timesteps) is about two times greater in the HD regions. This can explain the flatter profile of the GSMF with respect to the LD regions. The relevance of mergers is also discussed with a different approach in the next section.

## 5.2. An empirical approach

We used VIPERS data to test the empirical description of galaxy evolution proposed by P10, in which the galaxy number density changes as a function of  $M$ , SFR, and environment. Three observational facts are fundamental in P10 because

- 1) the stellar mass function of star-forming galaxies has the same shape at different redshifts (i.e.  $\alpha$  and  $M_\star$  are nearly constant, see e.g. [Ilbert et al. 2010](#)), with little increase in normalisation moving towards lower redshifts;
- 2) there is a tight relation between SFR and stellar mass for star-forming galaxies (the so-called main sequence) with  $SFR \propto M^{1+\beta}$  (e.g. [Noeske et al. 2007](#); [Elbaz et al. 2007](#); [Daddi et al. 2007](#));
- 3) average sSFR can be parametrised with respect to stellar mass and redshift/cosmic time ([Speagle et al. 2014](#), and references therein), while it is independent of environment (P10; [Muzzin et al. 2012](#); [Wetzel et al. 2012](#)).

In spite of the strong consensus in the literature, we caution that these three findings have been established only recently and that new data may be at odds with them, bringing the basis of [Peng et al.](#) work into question. For instance, [Ilbert et al. \(2015\)](#) show that  $\log(SFR) \propto -M \log(M)$  is a better parametrisation than 2), at least for their 24  $\mu\text{m}$  selected sample.

The keystone of P10 description is that two mechanisms can regulate the decline of star formation; they are named *mass quenching* and *environment quenching* because they depend on  $M$  and  $\delta$ , respectively. In a first approximation, the evolution of the GSMF can be parametrised by the two mechanisms. As we show below, other processes are needed in the HD regions. Using data from the local Universe (SDSS-DR7, [Abazajian et al. 2009](#)) and at  $z \sim 1$  (zCOSMOS, [Lilly et al. 2007](#)), the authors argue that mass and environment quenching are fully separable. The effect of both can be expressed analytically; in particular, the mass quenching rate is

$$\lambda_m = \frac{SFR}{M_\star} = \mu SFR, \quad (6)$$

where  $M_\star$  (namely the Schechter parameter of the star-forming mass function) is constant ( $M_\star \equiv \mu^{-1} \approx 10^{10.6} M_\odot$ , according to observations). Equation (6) can be regarded as the probability that a galaxy becomes passive via mass quenching. This is the simplest analytical form that satisfies 1)–3) but alternative, more complex formulations cannot be excluded.

The empirical laws of P10 do not shed light on the physical processes responsible for quenching but describe its characteristics. In [Peng et al. \(2012\)](#), mass and environment quenching are linked to halo occupation. In this view, central galaxies are subjected to the former, which is analogous to the “internal quenching” described in other papers (e.g. [Gabor et al. 2010](#); [Woo et al. 2012](#), and reference therein), while environment quenching is the preferred channel of satellite galaxies. This distinction however is not clear-cut because satellite galaxies can spend a significant portion of their lives as centrals, before being accreted into another halo (see e.g. [De Lucia et al. 2012](#)). Moreover, using

the same SDSS group catalogue of [Peng et al. \(2012\)](#), [Knobel et al. \(2015\)](#) show that the central vs. satellite dichotomy disappears when excluding isolated galaxies from the sample of central galaxies (i.e. central galaxies in groups are affected by the environment in the same way as satellites).

With these simple prescriptions, it is possible to reproduce several statistics of galaxies across cosmic time. In P10, the authors generate a galaxy sample at  $z = 10$  with a primordial stellar mass function that follows a power law, and they evolve it down to  $z = 0$ . That mock sample has very simple features, e.g. active galaxies form stars at a constant level that is given by the sSFR( $z, M$ ) parametrisation of [Pannella et al. \(2009\)](#). At any epoch, a fraction of blue galaxies become red, proportionally to mass and environment quenching rates. This picture does not include the birth of new galaxies.

Here, we do not make use of mock galaxies, but rather start from the observed stellar mass function in a given  $z$ -bin and “evolve” it to a lower redshift following the prescriptions of P10. Then, we compare such an “empirical prediction” of the GSMF with our data.

In the LD regions, the fraction of VIPERS active galaxies that migrate into the passive mass function is assumed  $\propto \lambda_m$ ; i.e. it is determined by mass quenching alone. To evaluate the number of new quenched galaxies, one has to insert a functional form of the specific SFR, generally speaking sSFR( $z, M$ ), into Eq. (6). The function chosen by P10 (their Eq. (1)) comes from [Pannella et al. \(2009\)](#). From such a definition of the quenching rate, it follows that, in a given mass bin centred on  $M_b$ , the galaxy number density evolution is

$$\begin{aligned} \Phi_{\text{pass}}(z_2) &= \Phi_{\text{pass}}(z_1) + \int_{t(z_1)}^{t(z_2)} \Phi_{\text{act}}(z) \lambda_m dt \\ &= \Phi_{\text{pass}}(z_1) + \tilde{\Phi}_{\text{act}} \mu \int_{z_1}^{z_2} M_b sSFR(z, M_b) dz. \end{aligned} \quad (7)$$

In this equation, the GSMF of the active sample is constant ( $\tilde{\Phi}_{\text{act}}$ ) between  $z_1$  and  $z_2 < z_1$ , regardless of the environment in which it is computed. This assumption is supported both by our data (see Fig. 3) and other studies (e.g. [Pozzetti et al. 2010](#); [Ilbert et al. 2013](#));  $\tilde{\Phi}_{\text{act}}$  is determined by averaging the  $\Phi_{\text{act}}$  estimates at  $z_1$  and  $z_2$ . We apply Eq. (7) in the LD environment, evolving data at  $0.8 < z \leq 0.9$  down to  $\langle z \rangle = 0.72$  and  $\langle z \rangle = 0.6$ . The resulting passive GSMFs, built under the action of mass quenching alone, are consistent with those observed in the corresponding redshift bins (see Fig. 9, upper panels). We repeat the procedure starting from  $0.65 < z < 0.8$ , finding good agreement at  $\langle z \rangle = 0.6$ . (This comparison is not shown in the figure.)

The major uncertainty in this technique is related to SFR- $M$  relation. To quantify the impact of different parametrisations, we also used, instead of the equation provided in P10, the “concordance function” obtained by [Speagle et al. \(2014\)](#) when fitting data of 25 studies from the literature (see their Eq. (28)). We also estimated the uncertainty related to  $\tilde{\Phi}_{\text{act}}$  by replacing it with upper and lower values of  $\Phi_{\text{act}}(z_1)$  and  $\Phi_{\text{act}}(z_2)$ , respectively. We note that keeping the active mass function fixed introduces a much smaller uncertainty with respect to the sSFR( $z, M$ ) parametrisation. Another approximation in the procedure is that galaxies do not change environment as time goes by. This assumption is appropriate in the time interval we probe, as we verified following the evolution of mock galaxies in the simulations of Sect. 5.1.

We also applied Eq. (7) in the HD regions. We emphasise that in this case there should be a combined effect of both mass and environment quenching mechanisms. However, P10 show

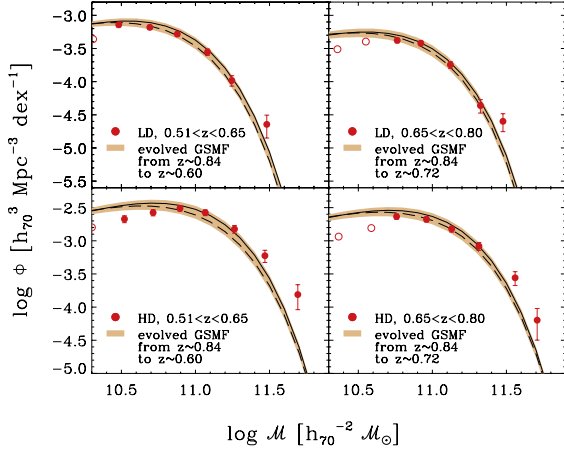


**Fig. 9.** Comparison between the GSMFs constructed with the P10 recipe and the VIPERS data. In each panel, red filled circles indicate the  $1/V_{\max}$  points (with Poissonian errors) of the VIPERS passive mass function in the redshift bin and environment indicated in the legend. Lines and shaded areas represent the evolution of the GSMF observed at  $0.8 < z < 0.9$ , down to the same redshift as the plotted data points. Applying the quenching description of P10, we obtain two different estimates if we use the original  $sSFR(z, M)$  parametrisation of P10 (solid line) or the function provided in [Speagle et al. \(2014\)](#), dashed line). Another error is introduced to account for the uncertainties in the integration (see Eq. (6)), giving the final width of the shaded area.

that the former is more effective at  $\log(M/M_{\odot}) < 10.5$ , and therefore negligible in the VIPERS stellar mass range. The main difference with respect to LD, instead, is that after becoming passive, galaxies in the overdensities have a greater chance of merging. We show that such dry mergers are crucial to modifying the shape of the passive GSMF. In fact, a description that only accounts for mass quenching does not reproduce the passive mass function of HD galaxies well (Fig. 9, lower panels). Dry mergers produce a redistribution of the stellar mass in the simulated GSMF, which is now more consistent with the observed one (Fig. 10). We add this “post-quenching” ingredient (i.e. dry merging) through the scheme described below.

P10 assume a simple model in which part of the passive population merges with 1:1 mass ratio. Similar prescriptions are also used in the “backward evolutionary model” of [Boissier et al. \(2010\)](#). Both P10 and [Boissier et al. \(2010\)](#) find that dry major mergers enhance the exponential tail of the passive GSMF and make  $M_{\star}$  increase with respect to the LD environment. They also consider minor mergers to be fully negligible in the GSMF evolution, at least at  $M \geq 10^{10} M_{\odot}$  (see also [López-Sanjuan et al. 2011](#); [Ferreras et al. 2014](#)). In our analysis, we introduce dry (major) mergers in the evolution of  $\Phi_{\text{pass,HD}}$ , assuming that two objects in the same bin of  $\log M$  can merge without triggering relevant episodes of star formation (e.g. [Di Matteo et al. 2005](#); [Karman et al. 2015](#)). We set the fraction of galaxies undergoing a 1:1 merger to be equal to  $f_{\text{dry}}(z)$ , with no dependence on the stellar mass of the initial pair ([Xu et al. 2012](#)). An estimate of  $f_{\text{dry}}(z)$  is inferred by [Man et al. \(2014\)](#) by counting galaxy pairs with stellar mass ratio less than 1:4<sup>13</sup>.

<sup>13</sup> [Man et al.](#) show that their merger rate is suitable to studying dry mergers; e.g., it is consistent with that of gas-poor galaxies in the simulations of [Hopkins et al. \(2010\)](#). Moreover, the analysis of these authors is performed on the COSMOS field, so it can be easily compared to several previous studies (e.g. [de Ravel et al. 2011](#); [Xu et al. 2012](#); [López-Sanjuan et al. 2012](#)), with which they are in fairly good agreement. P10 use the merger rate derived by [de Ravel et al. \(2011\)](#) for the  $z$ COSMOS galaxies.

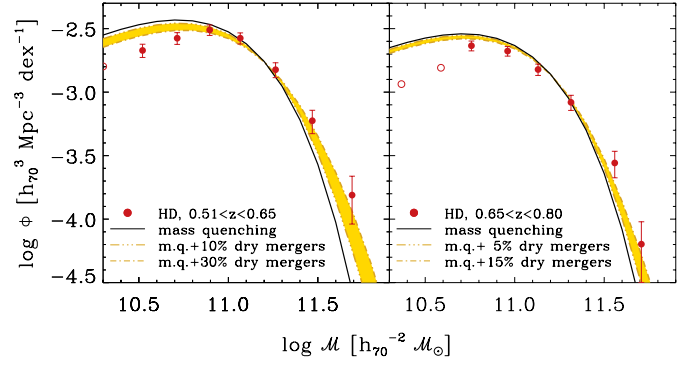


**Fig. 10.** Evolution of the passive mass function in the HD environment, including dry mergers. The solid line in each panel is the predicted GSMF in the HD environment, as in Fig. 9, assuming only mass quenching and the sSFR parametrisation of P10; yellow shaded area is the GSMF modified by dry mergers, whose percentage ranges from 5–10% (triple-dot-dashed line) to 15–30% (dot-dashed line) depending on the redshift bin. In each  $z$ -bin, red circles are the  $1/V_{\max}$  estimates (with Poissonian errors) of the stellar mass function of the VIPERS passive galaxies (symbols are filled above the completeness limit  $M_{\text{lim}}^{\text{pass}}$ ).

The merger rate of [Man et al. \(2014\)](#) leads to a merger fraction  $f_{\text{dry}} = 5^{+3}_{-2}\%$  from  $\langle z \rangle = 0.84$  to  $0.72$  and  $f_{\text{dry}} = 10^{+6}_{-4}\%$  from  $\langle z \rangle = 0.84$  to  $0.6$ . Since they are averaged over the general COSMOS field, these values can get to be about two to three times higher in HD environments ([Kampczyk et al. 2013](#); see also [Lin et al. 2010](#); [Lotz et al. 2013](#)). For this reason we test a range of  $f_{\text{dry}}$  values: from 5% to 15% in the time span from  $\langle z \rangle = 0.84$  to  $0.72$  ( $\sim 0.7$  Gyr) and 10–30% from redshift 0.84 to  $0.6$  (i.e. across  $\sim 1.4$  Gyr). As stressed above, dry merging is the key element for reconciling the simulated GSMF with the observed one (Fig. 10). Nevertheless, a  $1\sigma$  difference remains at  $\log(M/M_{\odot}) \approx 10.4$ . Together with the ( $<1\sigma$ ) difference at the high-mass end, this overestimate may suggest that the impact of mergers in the densest regions of VIPERS could be even greater than what we assumed. At the same time, we cannot exclude that the explanation for these (minor) tensions resides in the simplicity of our parametrisation. Indeed the result depends on the model used to describe the evolution of these massive galaxies. For example, central ones could grow significantly by (multiple) accretion of satellites. Since our sample does not distinguish between satellite and central galaxies, we could not test this scenario.

## 6. Conclusions

Along with the accuracy of redshift measurements, the large volume probed makes VIPERS the ideal survey for studying environmental effects at intermediate redshifts. We reconstructed the local density field ([Cucciati et al. 2014](#); Cucciati et al., in prep.) and identified galaxies embedded in under- and overdensities. We estimated the volumes occupied by such LD and HD regions, finding that they represent nearly 50% and 7% of the total comoving volume of the survey. Thanks to the volume reconstruction, we could properly compute the number density of galaxies in these two opposite environments and compare the GSMFs at different epochs.

The stellar mass function of LD galaxies is nearly constant in the redshift range  $0.51 < z < 0.9$ , while a significant evolution is observed in the HD regions. Moreover, we found that the VIPERS stellar mass function has a shape that depends on the environment, with a higher number of massive objects in the

overdensities. Interestingly, our approach is complementary to the other VIPERS studies that show the increase in the galaxy bias as a function of  $M$  (e.g. Marulli et al. 2013). Despite our completeness limit ( $M_{\text{lim}} \gtrsim 10.4$  at  $z \sim 0.6$ ), we also found hints that the low-mass end of the GSMF is flatter in the HD regions with a particular decrement of the passive sample. This marginal effect could be robustly assessed once the final VIPERS catalogues ( $\sim 90\,000$  spectra) are available.

The LD vs. HD variance is quantitatively described by the Schechter (1976) parameters: the  $\alpha$ - $M_*$  likelihood contours from the STY fit show a significant difference between the two environments. In particular, the enhancement of the GSMF massive end is described well by  $M_*$ , which increases by  $\sim 0.25$  dex in the HD regions (namely  $0.24 \pm 0.12$ ,  $0.27 \pm 0.15$ , and  $0.21 \pm 0.11$  dex at  $z \sim 0.6$ ,  $0.72$ , and  $0.84$ , respectively). Such a difference remains visible when considering only the active or the passive sample. An environmental imprint in the stellar mass function has already been observed in the local Universe (Baldry et al. 2006; Peng et al. 2010). With VIPERS, it also becomes evident for the first time at  $z \gtrsim 0.5$ .

We investigated these environmental trends by using ten mock catalogues derived from the Millennium simulation. Galaxies were simulated following the prescriptions of De Lucia & Blaizot (2007) and the survey design is reproduced to make these catalogues similar to VIPERS. In this way we were able to define galaxy environments as done in the real survey. The different slope of the low-mass end is also observed in the mock GSMF and can be associated to a larger number of merger events where the local galaxy density is higher. Looking at the exponential tail of the mock GSMF, the higher number density of  $M > M_*$  galaxies in the HD regions is linked to a large number of haloes with  $M_{\text{halo}} > 10^{13} M_{\odot}$ . Such massive haloes are absent in the LD sample. As a result, both satellite and merger fractions increase when selecting denser environments. To summarise, our classification based on the galaxy density contrast corresponds to a distinction in halo properties, highlighting the ambiguity of the “mass vs. environment” dichotomy (see De Lucia et al. 2012).

We found that the difference between LD and HD mass functions decreases from  $\langle z \rangle = 0.60$  to  $0.84$ . The trend is expected to continue at higher redshifts, where the massive haloes that characterise our densest environment have not collapsed yet. We could connect our results to the analysis of Mortlock et al. (2014), in which the GSMF at  $1 < z < 1.5$  does not change when computed in either high or low densities (even though the large uncertainties could hide some minor environmental effect). This change can be linked to the different conditions of cosmological structures in the earlier stages of the Universe, with group environment being more effective at  $z < 1$ .

We also experimented with the empirical description of Peng et al. (2010), in which the stellar mass function of passive galaxies evolves under the combined effect of mass and environment quenching. Unlike other studies, we used this approach in a self-consistent way: we evolve the observed mass function at each redshift bin considered in our study and compare the expectation to the GSMF observed at the lower redshift bin. Our results show that the measured evolution of the GSMF in low-density regions is consistent with a model in which galaxy evolution is dominated by internal physical processes alone (“mass quenching” in the formalism by Peng et al.). For high-density regions, however, additional processes have to be considered to explain the evolution of the massive end of the GSMF. In particular, we demonstrated that the observed evolution can be explained by including the effect of dry mergers.

We stress that our survey has the ability to shed light on the role of mergers in shaping the GSMF, such as tackling the problem of sample variance highlighted by Keenan et al. (2014). Moreover, in the redshift range of our survey, merging events are more frequent than in the local Universe (López-Sanjuan et al. 2012; but see also outcomes from state-of-the-art simulations in Rodríguez-Gomez et al. 2015). In our study, both semi-analytic modelling and empirical approaches highlighted the importance of mergers in the large-scale dense environment. Future analyses relying on the final  $24 \text{ deg}^2$  release of VIPERS will complement the present results, providing further details about galaxy-galaxy interactions.

**Acknowledgements.** We acknowledge the crucial contribution of the ESO staff for managing service observations. In particular, we are deeply grateful to M. Hilker for his constant help and support of this program. Italian participation in VIPERS has been funded by INAF through PRIN 2008 and 2010 programmes. O.C. acknowledges the support from grants ASI-INAf I/023/12/0 “Attività relative alla fase B2/C per la missione Euclid”. L.G. and B.R.G. acknowledge support of the European Research Council through the Darklight E.R.C. Advanced Research Grant (# 291521). O.L.F. acknowledges the support of the European Research Council through the EARLY ERC Advanced Research Grant (# 268107). A.P., K.M., and J.K. have been supported by the National Science Centre (grants UMO-2012/07/B/ST9/04425 and UMO-2013/09/D/ST9/04030), the Polish-Swiss Astro Project (co-financed by a grant from Switzerland through the Swiss Contribution to the enlarged European Union). R.T. acknowledges financial support from the European Research Council under the European Community’s Seventh Framework Programme (FP7/2007-2013)/ERC grant agreement n. 202686. E.B., F.M., and L.M. acknowledge the support from grants ASI-INAf I/023/12/0 and PRIN MIUR 2010-2011. LM also acknowledges financial support from PRIN INAF 2012. Y.M. acknowledges support from CNRS/INSU (Institut National des Sciences de l’Univers) and the Programme National Galaxies et Cosmologie (PNCG). The research was conducted within the framework of the HECOLS International Associated Laboratory, supported in part by the Polish NCN grant DEC-2013/08/M/ST9/00664.

## References

- Abazajian, K. N., Adelman-McCarthy, J. K., Agüeros, M. A., et al. 2009, *ApJS*, **182**, 543
- Abbas, U., & Sheth, R. K. 2005, *MNRAS*, **364**, 1327
- Abbas, U., & Sheth, R. K. 2006, *MNRAS*, **372**, 1749
- Amara, A., Lilly, S., Kovac, K., et al. 2012, *MNRAS*, **12**
- Annunziatella, M., Biviano, A., Mercurio, A., et al. 2014, *A&A*, **571**, A80
- Annunziatella, M., Mercurio, A., Biviano, A., et al. 2016, *A&A*, **585**, A160
- Arnouts, S., Le Floch, E., Chevallard, J., et al. 2013, *A&A*, **67**, 1
- Baldry, I., Balogh, M., Bower, R., et al. 2006, *MNRAS*, **373**, 469
- Baldry, I., Driver, S., Loveday, J., et al. 2012, *MNRAS*, **421**, 621
- Bassett, R., Papovich, C., Lotz, J. M., et al. 2013, *ApJ*, **770**, 58B
- Bernardi, M., Meert, A., Sheth, R. K., et al. 2013, *MNRAS*, **436**, 697
- Bertin, E., & Arnouts, S. 1996, *A&AS*, **117**, 393
- Blanton, M. R., & Moustakas, J. 2009, *ARA&A*, **47**, 159
- Boissier, S., Buat, V., & Ilbert, O. 2010, *A&A*, **522**, A18
- Bolzonella, M., Miralles, J.-M., & Pelló, R. 2000, *A&A*, **363**, 476
- Bolzonella, M., Kovač, K., Pozzetti, L., et al. 2010, *A&A*, **524**, A76
- Boselli, A., & Gavazzi, G. 2006, *PASP*, **118**, 517
- Bouchet, P., Lequeux, J., Maurice, E., Prevot, L., & Prevot-Burnichon, M. 1985, *A&A*, **149**, 330
- Brammer, G. B., Whitaker, K. E., van Dokkum, P. G., et al. 2009, *ApJ*, **706**, L173
- Bruzual, G., & Charlot, S. 2003, *MNRAS*, **344**, 1000
- Bundy, K., Ellis, R., Conselice, C., et al. 2006, *ApJ*, **651**, 120
- Burton, C. S., Jarvis, M. J., Smith, D. J. B., et al. 2013, *MNRAS*, **433**, 771
- Calvi, R., Poggianti, B. M., Vulcani, B., & Fasano, G. 2013, *MNRAS*, **432**, 3141
- Calzetti, D., Armus, L., Bohlin, R., et al. 2000, *ApJ*, **533**, 682
- Cappellari, M., Emsellem, E., Krajnovi, D., et al. 2011, *MNRAS*, **416**, 1680
- Cappi, A., Marulli, F., Bel, J., et al. 2015, *A&A*, **579**, A70
- Chabrier, G. 2003, *PASP*, **115**, 763
- Chevallard, J., Charlot, S., Wandelt, B., & Wild, V. 2013, *MNRAS*, **432**, 2061
- Cirasuolo, M., McLure, R., Dunlop, J., et al. 2010, *MNRAS*, **401**, 1166
- Conroy, C., Gunn, J., & White, M. 2009, *ApJ*, **699**, 486
- Cooper, M., Newman, J., Madgwick, D., et al. 2005, *ApJ*, **634**, 833
- Cooper, M., Newman, J., Weiner, B., et al. 2008, *MNRAS*, **383**, 1058
- Coupon, J., Ilbert, O., Kilbinger, M., et al. 2009, *A&A*, **500**, 981
- Cucciati, O., Iovino, A., Marinoni, C., et al. 2006, *A&A*, **458**, 39



- Cucciati, O., Iovino, A., Kovac, K., et al. 2010, *A&A*, **524**, A2
- Cucciati, O., De Lucia, G., Zucca, E., et al. 2012, *A&A*, **548**, A108
- Cucciati, O., Granett, B. R., Branchini, E., et al. 2014, *A&A*, **565**, A67
- Daddi, E., Dickinson, M., Morrison, G., et al. 2007, *ApJ*, **670**, 156
- Darvish, B., Mobasher, B., Sobral, D., Scoville, N., & Aragon-Calvo, M. 2015, *ApJ*, **805**, 121
- Davidzon, I., Bolzonella, M., Coupon, J., et al. 2013, *A&A*, **558**, A23
- Davis, M., & Geller, M. J. 1976, *ApJ*, **208**, 13
- de la Torre, S., Guzzo, L., Kovač, K., et al. 2010, *MNRAS*, **409**, 867
- de la Torre, S., Guzzo, L., Peacock, J., et al. 2013, *A&A*, **557**, A54
- De Lucia, G., & Blaizot, J. 2007, *MNRAS*, **375**, 2
- De Lucia, G., Weinmann, S., Poggianti, B. M., Aragón-Salamanca, A., & Zaritsky, D. 2012, *MNRAS*, **423**, 1277
- de Ravel, L., Kampezyk, P., Le Fèvre, O., et al. 2011 unpublished [[arXiv:1104.5470](#)]
- Di Matteo, T., Springel, V., & Hernquist, L. 2005, *Nature*, **433**, 604
- Di Porto, C., Branchini, E., Bel, J., et al. 2014, *A&A*, submitted [[arXiv:1406.6692](#)]
- Dressler, A. 1980, *ApJ*, **236**, 351
- Efstathiou, G., Ellis, R. S., & Peterson, B. A. 1988, *MNRAS*, **232**, 431
- Elbaz, D., Daddi, E., Le Borgne, D., et al. 2007, *A&A*, **468**, 33
- Ferreras, I., Trujillo, I., Marmol-Queraltó, E., et al. 2014, *MNRAS*, **444**, 906
- Fontana, A., Pozzetti, L., Donnarumma, I., et al. 2004, *A&A*, **424**, 23
- Fontanot, F., De Lucia, G., Monaco, P., Somerville, R., & Santini, P. 2009, *MNRAS*, **397**, 1776
- Fossati, M., Wilman, D. J., Fontanot, F., et al. 2015, *MNRAS*, **446**, 2582
- Fritz, A., Ziegler, B. L., Bower, R. G., Smail, I., & Davies, R. L. 2005, *MNRAS*, **358**, 233
- Fritz, A., Scoddeggio, M., Ilbert, O., et al. 2014, *A&A*, **563**, A92
- Gabor, J., Davé, R., Finlator, K., & Oppenheimer, B. 2010, *MNRAS*, **407**, 749
- Garilli, B., Paiono, L., Scoddeggio, M., et al. 2012, *PASP*, **124**, 1232
- Garilli, B., Guzzo, L., Scoddeggio, M., et al. 2014, *A&A*, **562**, A23
- Giodini, S., Finoguenov, A., Pierini, D., et al. 2012, *A&A*, **538**, A104
- Granett, B., Branchini, E., Guzzo, L., et al. 2015, *A&A*, **583**, A61
- Grützbauch, R., Conselice, C. J., Varela, J., et al. 2011, *MNRAS*, **411**, 929
- Guo, Q., White, S., Boylan-Kolchin, M., et al. 2011, *MNRAS*, **413**, 101
- Guo, Q., White, S., Angulo, R. E., et al. 2013, *MNRAS*, **428**, 1351
- Guzzo, L., Scoddeggio, M., Garilli, B., et al. 2014, *A&A*, **566**, A108
- Haas, M. R., Schaye, J., & Jeason-Daniel, A. 2012, *MNRAS*, **419**, 2133
- Hahn, C., Blanton, M., Moustakas, J., et al. 2015, *ApJ*, **806**, 162
- Hearin, A. P., Behroozi, P. S., & van den Bosch, F. C. 2015, *MNRAS*, submitted ArXiv e-prints [[arXiv:1504.05578](#)]
- Hinshaw, G., Larson, D., Komatsu, E., et al. 2013, *ApJS*, **208**, 19
- Hopkins, P. F., Bundy, K., Croton, D., et al. 2010, *ApJ*, **715**, 202
- Ilbert, O., Tresse, L., Arnouts, S., et al. 2004, *MNRAS*, **351**, 541
- Ilbert, O., Tresse, L., Zucca, E., et al. 2005, *A&A*, **439**, 863
- Ilbert, O., Salvato, M., Le Floc'h, E., et al. 2010, *ApJ*, **709**, 644
- Ilbert, O., McCracken, H. J., Le Fèvre, O., et al. 2013, *A&A*, **556**, A55
- Ilbert, O., Arnouts, S., Floc'h, E. L., et al. 2015, *A&A*, **24**
- Kampezyk, P., Lilly, S. J., de Ravel, L., et al. 2013, *ApJ*, **762**, 43
- Karman, W., Maccio, A. V., Kannan, R., Moster, B. P., & Somerville, R. S. 2015, *MNRAS*, **452**, 2984
- Kauffmann, G., Heckman, T., White, S., et al. 2003, *MNRAS*, **341**, 33
- Kauffmann, G., White, S. D. M., Heckman, T. M., et al. 2004, *MNRAS*, **353**, 713
- Keenan, R. C., Foucaud, S., De Propris, R., et al. 2014, *ApJ*, **795**, 157
- Knobel, C., Lilly, S. J., Woo, J., & Kovac, K. 2015, *ApJ*, **800**, 24
- Kovač, K., Lilly, S., Cucciati, O., et al. 2010a, *ApJ*, **708**, 505
- Kovač, K., Lilly, S., Knobel, C., et al. 2010b, *ApJ*, **718**, 86
- Le Fèvre, O., Saisse, M., Mancini, D., et al. 2003, in *Instrument Design and Performance for Optical/Infrared Ground-based Telescopes*, eds. M. Iye, & A. F. M., Moorwood, SPIE, **4841**, 1670
- Le Fèvre, O., Vettolani, G., Garilli, B., et al. 2005, *A&A*, **439**, 845
- Lee, S.-K., Idzi, R., Ferguson, H., et al. 2009, *ApJS*, **184**, 100
- Lilly, S., Le Fèvre, O., Renzini, A., et al. 2007, *ApJS*, **172**, 70
- Lin, L., Cooper, M. C., Jian, H.-Y., et al. 2010, *ApJ*, **718**, 1158
- López-Sanjuan, C., Le Fèvre, O., de Ravel, L., et al. 2011, *A&A*, **530**, A20
- López-Sanjuan, C., Le Fèvre, O., Ilbert, O., et al. 2012, *A&A*, **548**, A7
- Lotz, J. M., Papovich, C., Faber, S. M., et al. 2013, *ApJ*, **773**, 154
- Lu, T., Gilbank, D. G., McGee, S. L., Balogh, M. L., & Gallagher, S. 2012, *MNRAS*, **420**, 126
- Lu, Y., Wechsler, R. H., Somerville, R. S., et al. 2014, *ApJ*, **795**, 123
- Małek, K., Solarz, A., Pollo, A., et al. 2013, *A&A*, **557**, A16
- Man, A. W. S., Zirm, A. W., & Toft, S. 2014, *ApJ*, submitted [[arXiv:1410.3479](#)]
- Maraston, C., Pforr, J., Henriques, B. B. M., et al. 2013, *MNRAS*, **435**, 2764
- Marchesini, D., van Dokkum, P., Förster Schreiber, N., et al. 2009, *ApJ*, **701**, 1765
- Marchetti, A., Granett, B., Guzzo, L., et al. 2013, *MNRAS*, **428**, 1424
- Marinoni, C., Davis, M., Newman, J. A., & Coil, A. L. 2002, *ApJ*, **580**, 122
- Marulli, F., Bolzonella, M., Branchini, E., et al. 2013, *A&A*, **557**, A17
- McGee, S. L., Balogh, M. L., Bower, R. G., Font, A. S., & McCarthy, I. G. 2009, *MNRAS*, **400**, 937
- Mitchell, P. D., Lacey, C. G., Baugh, C. M., & Cole, S. 2013, *MNRAS*, **435**, 87
- Mo, H. J., & White, S. D. M. 1996, *MNRAS*, **282**, 347
- Mobasher, B., Dahlen, T., Ferguson, H. C., et al. 2015, *ApJ*, **808**, 101
- Moresco, M., Pozzetti, L., Cimatti, A., et al. 2013, *A&A*, **558**, A61
- Mortlock, A., Conselice, C. J., Hartley, W. G., et al. 2014, *MNRAS*, **447**, 2
- Moster, B., Somerville, R., Newman, J., & Rix, H.-W. 2011, *ApJ*, **731**, 113
- Moustakas, J., Coil, A., Aird, J., et al. 2013, *ApJ*, **767**, 50
- Muldrew, S. I., Croton, D. J., Skibba, R. A., et al. 2012, *MNRAS*, **419**, 2670
- Muzzin, A., Wilson, G., Yee, H. K. C., et al. 2012, *ApJ*, **746**, 188
- Noeske, K., Weiner, B., Faber, S., et al. 2007, *ApJ*, **660**, L43
- Oemler, A. 1974, *ApJ*, **194**, 1
- Oke, J. 1974, *ApJS*, **27**, 21
- Pannella, M., Carilli, C. L., Daddi, E., et al. 2009, *ApJ*, **698**, L116
- Pasquali, A., van den Bosch, F. C., Mo, H. J., Yang, X., & Somerville, R. 2009, *MNRAS*, **394**, 38
- Peng, Y.-J., Lilly, S., Kovač, K., et al. 2010, *ApJ*, **721**, 193
- Peng, Y.-J., Lilly, S. J., Renzini, A., & Carollo, M. 2012, *ApJ*, **757**, 4
- Planck Collaboration XIII. 2015, *A&A*, submitted [[arXiv:1502.01589](#)]
- Popesso, P., Biviano, A., Finoguenov, A., et al. 2015, *A&A*, **579**, A132
- Postman, M., & Geller, M. J. 1984, *ApJ*, **281**, 95
- Pozzetti, L., Bolzonella, M., Lamareille, F., et al. 2007, *A&A*, **474**, 443
- Pozzetti, L., Bolzonella, M., Zucca, E., et al. 2010, *A&A*, **523**, A13
- Prevot, M., Lequeux, J., Prevot, L., Maurice, E., & Rocca-Volmerange, B. 1984, *A&A*, **132**, 389
- Rodriguez-Gomez, V., Genel, S., Vogelsberger, M., et al. 2015, *MNRAS*, **449**, 49
- Salim, S., Charlot, S., Rich, R. M., et al. 2005, *ApJ*, **619**, L39
- Sandage, A., & Visvanathan, N. 1978, *ApJ*, **225**, 742
- Sandage, A., Tammann, G. A., & Yahil, A. 1979, *ApJ*, **232**, 352
- Schechter, P. 1976, *ApJ*, **203**, 297
- Schmidt, M. 1968, *ApJ*, **151**, 393
- Scoddeggio, M., Vergani, D., Cucciati, O., et al. 2009, *A&A*, **501**, 21
- Scoville, N., Arnouts, S., Aussel, H., et al. 2013, *ApJ*, **206**, 3
- Smith, G., Treu, T., Ellis, R., Moran, S., & Dressler, A. 2005, *ApJ*, **620**, 78
- Speagle, J. S., Steinhart, C. L., Capak, P. L., & Silverman, J. D. 2014, *ApJS*, **214**, 15
- Spergel, D. N., Verde, L., Peiris, H. V., et al. 2003, *ApJS*, **148**, 175
- Spergel, D. N., Bean, R., Dore, O., et al. 2007, *ApJS*, **170**, 377
- Springel, V., White, S., Jenkins, A., et al. 2005, *Nature*, **435**, 629
- Takada, M., Ellis, R. S., Chiba, M., et al. 2014, *PASJ*, **66**, R1
- Thomas, D., Maraston, C., Schawinski, K., Sarzi, M., & Silk, J. 2010, *MNRAS*, **404**, 1775
- van den Bosch, F., Aquino, D., Yang, X., et al. 2008, *MNRAS*, **387**, 79
- van der Burg, R. F. J., Muzzin, A., Hoekstra, H., et al. 2013, *A&A*, **557**, A15
- van der Wel, A., Bell, E., Holden, B., Skibba, R., & Rix, H.-W. 2010, *ApJ*, **714**, 1779
- Vulcani, B., Poggianti, B. M., Fasano, G., et al. 2012, *MNRAS*, **420**, 1481
- Vulcani, B., Poggianti, B., Oemler, A., et al. 2013, *A&A*, **550**, A58
- Wang, J., De Lucia, G., Kitzbichler, M. G., & White, S. D. M. 2008, *MNRAS*, **384**, 1301
- Weinmann, S., van den Bosch, F., Yang, X., et al. 2006, *MNRAS*, **372**, 1161
- Weinzierl, S. 2000, Arxiv e-prints, [[arXiv:hep-ph/000](#)]
- Wetzel, A. R., Tinker, J. L., & Conroy, C. 2012, *MNRAS*, **424**, 232
- Whitaker, K. E., Labbé, I., van Dokkum, P. G., et al. 2011, *ApJ*, **735**, 86
- Williams, R. J., Quadri, R. F., Franx, M., van Dokkum, P., & Labbé, I. 2009, *ApJ*, **691**, 1879
- Woo, J., Dekel, A., Faber, S. M., et al. 2012, *MNRAS*, **428**, 3306
- Xu, C. K., Zhao, Y., Scoville, N., et al. 2012, *ApJ*, **747**, 85
- Zahid, H., Kewley, L., & Bresolin, F. 2011, *ApJ*, **730**, 137
- Zucca, E., Bardelli, S., Bolzonella, M., et al. 2009, *A&A*, **508**, 1217

<sup>1</sup> Aix-Marseille Université, CNRS, LAM (Laboratoire d'Astrophysique de Marseille) UMR 7326, 13388 Marseille, France  
e-mail: iary.davidzon@lam.fr

<sup>2</sup> INAF-Osservatorio Astronomico di Bologna, via Ranzani 1, 40127, Bologna, Italy

<sup>3</sup> Dipartimento di Fisica e Astronomia–Alma Mater Studiorum Università di Bologna, viale Berti Pichat 6/2, 40127 Bologna, Italy

<sup>4</sup> INAF-Osservatorio Astronomico di Trieste, via G. B. Tiepolo 11, 34143 Trieste, Italy

- <sup>5</sup> Canada-France-Hawaii Telescope, 65–1238 Mamalahoa Highway, Kamuela, HI 96743, USA
- <sup>6</sup> INAF–Istituto di Astrofisica Spaziale e Fisica Cosmica Milano, via Bassini 15, 20133 Milano, Italy
- <sup>7</sup> INAF–Osservatorio Astronomico di Brera, via Brera 28, 20122 Milano, via E. Bianchi 46, 23807 Merate, Italy
- <sup>8</sup> Dipartimento di Fisica, Università di Milano-Bicocca, Piazza della Scienza 3, 20126 Milano, Italy
- <sup>9</sup> INAF – Osservatorio Astronomico di Torino, 10025 Pino Torinese, Italy
- <sup>10</sup> Université de Toulon, CNRS, CPT, UMR 7332, 83957 La Garde, France
- <sup>11</sup> Aix-Marseille Université, CNRS, CPT, UMR 7332, 13288 Marseille, France
- <sup>12</sup> Dipartimento di Matematica e Fisica, Università degli Studi Roma Tre, via della Vasca Navale 84, 00146 Roma, Italy
- <sup>13</sup> INFN, Sezione di Roma Tre, via della Vasca Navale 84, 00146 Roma, Italy
- <sup>14</sup> INAF – Osservatorio Astronomico di Roma, via Frascati 33, 00040 Monte Porzio Catone (RM), Italy
- <sup>15</sup> Laboratoire Lagrange, UMR 7293, Université de Nice Sophia Antipolis, CNRS, Observatoire de la Côte d’Azur, 06300 Nice, France
- <sup>16</sup> Astronomical Observatory of the University of Geneva, Ch. d’Écogia 16, 1290 Versoix, Switzerland
- <sup>17</sup> Institut d’Astrophysique Spatiale, Université Paris-Sud, CNRS, UMR 8617, 91405 Orsay, France
- <sup>18</sup> Institute of Physics, Jan Kochanowski University, ul. Świetokrzyska 15, 25-406 Kielce, Poland
- <sup>19</sup> National Centre for Nuclear Research, ul. Hoza 69, 00-681 Warszawa, Poland
- <sup>20</sup> INFN, Sezione di Bologna, viale Berti Pichat 6/2, 40127 Bologna, Italy
- <sup>21</sup> Institute d’Astrophysique de Paris, UMR 7095 CNRS, Université Pierre et Marie Curie, 98bis boulevard Arago, 75014 Paris, France
- <sup>22</sup> Astronomical Observatory of the Jagiellonian University, Orla 171, 30-001 Cracow, Poland
- <sup>23</sup> Institute of Cosmology and Gravitation, Dennis Sciama Building, University of Portsmouth, Burnaby Road, Portsmouth, PO1 3FX
- <sup>24</sup> INAF–Istituto di Astrofisica Spaziale e Fisica Cosmica Bologna, via Gobetti 101, 40129 Bologna, Italy
- <sup>25</sup> INAF–Istituto di Radioastronomia, via Gobetti 101, 40129 Bologna, Italy

## Appendix A: Tests on the $1 + \delta$ distribution

In Sect. 3.1 we associated VIPERS galaxies to LD or HD environments by means of their density contrast  $\delta$ . Specifically, galaxies with  $\delta < 0.7$  are assumed to be in the LD region, while HD galaxies are those with  $\delta > 4$ . For the sake of clarity, we dub these thresholds  $\delta_{LD}$  and  $\delta_{HD}$ . Their respective values correspond to the 25th and 75th percentiles of the  $\delta$  distribution, which can be computed at various redshifts ( $0.51 < z \leq 0.65$ ,  $0.65 < z \leq 0.8$ ,  $0.8 < z \leq 0.9$ ) and in W1 and W4 separately. The final thresholds we adopted ( $\delta_{LD} = 0.7$ ,  $\delta_{HD} = 4$ ) were obtained by averaging the percentiles obtained in each bin. In this Appendix, we justify the choice of using constant values despite the small variations among different redshifts and fields (see Fig. 1).

First of all, we verify the absence of selection effects in the computation. Even though the selection of our spectroscopic targets, described through TSR, SSR, and CSR (Sect. 2.2), does vary with redshift, this is not the case for the mass-selected sample ( $\log(M/M_\odot) > 10.86$ ) we use as a proxy of the density field. The statistical weights of these galaxies are nearly constant from  $z = 0.51$  to  $0.9$ .

Some variation of  $\delta_{LD}$  and  $\delta_{HD}$  should be due to statistical fluctuations, since we are sampling a nearly Gaussian distribution (Di Porto et al. 2014) with a limited number of objects. In fact, each  $z$ -bin contains only galaxies that were spectroscopically observed, and the  $\delta$  ranking is sensitive to this incompleteness. From this perspective, the survey selection triggers some amount of scatter: datasets drawn from the same galaxy parent population can yield different quartile values just because they populate the tails of the original density distribution in different ways.

To verify this hypothesis, we performed a Monte Carlo simulation. First, we divided the VIPERS sample into the three  $z$ -bins mentioned above, keeping W1 and W4 separate. In each bin and for both fields individually, we derived a PDF from the observed  $\delta$  distribution. We extracted 100 000 times the same number of objects as observed in VIPERS and assigned a density contrast to these fake galaxies according to the reconstructed PDF. In other words, this task consists in reproducing the plot shown in Fig. 1 many times, as it would appear if we targeted different galaxies from the parent photometric sample (every time with the same sampling rate). The quartiles resulting from each realisation have a scatter in the range of 10–15% around the mean value.

Another reason for the fluctuations of  $\delta_{LD}$  and  $\delta_{HD}$  could be cosmic variance. In this case, it is not for the subsample of observed objects to vary but for the density field itself, e.g. because of field-to-field variations in large-scale clustering (Moster et al. 2011, and references therein). In VIPERS, this effect is generally small, thanks to its large volume, as shown in D13 and Fritz et al. (2014). To estimate the impact of cosmic variance on our definition of environment, we used two sets of simulations, each one consisting in ten independent mock galaxy catalogues. The first set comes from the halo occupation distribution (HOD) modelled by de la Torre et al. (2013; see also the description in Cucciati et al. 2014)<sup>14</sup>.

To do that, we started from mock catalogues that have 100% sampling rate, no masked area, and galaxy redshifts without observational errors (i.e. they are cosmological redshifts perturbed by peculiar velocities). We referred to them as “reference” mock catalogues. We manipulated them to reproduce the

VIMOS footprint and added redshift measuring errors to have the correct percentages of  $z_{\text{phot}}$  and  $z_{\text{spec}}$  (“VIPERS-like” mock catalogues). We estimated galaxy density contrast (through the projected 5NN, as described in Sect. 2.4), hence its distribution, in the three  $z$ -bins used in this work. Among the ten “VIPERS-like” realisations using HOD, the 25th (75th) percentile that determines the LD (HD) environment has  $\sim 5\%$  ( $\sim 10\%$ ) scatter. This outcome implies that the LD and HD thresholds in real data also vary because of cosmic variance. In the HOD mock catalogues the galaxy luminosity in the  $B$  band is available. Assuming an average  $M/L_B$  ratio, we estimated the fractional error due to cosmic variance in each bin of stellar mass of the total GSMF shown in Fig. 4.

In conclusion, the percentiles we estimated for VIPERS, in its two fields and within three different  $z$ -bins, spread over a range comparable to the one resulting in simulations. Undersampling of the  $\delta$  distribution and cosmic variance are what are mainly responsible for these fluctuations, which are small enough not to invalidate our choice of keeping  $\delta_{LD}$  and  $\delta_{HD}$  fixed.

We also verified that the galaxy density field does not evolve significantly from  $z = 0.9$  down to  $0.5$  (i.e. we can safely compare results obtained at different redshifts). In fact, the values of the density thresholds at the 25th and 75th percentiles do not show a dependence on  $z$ . Moreover, by means of cosmological simulations based on the Millennium Simulation (the same as used in Di Porto et al. 2014), we checked that the PDF of the underlying matter density field is almost constant between  $z = 1$  and  $0.5$ . These tests confirm that we can safely classify galaxies by using the same thresholds ( $\delta_{LD}$  and  $\delta_{HD}$ ) in different  $z$ -bins.

Besides that, we can estimate the purity and completeness of the LD and HD samples by means of the HOD simulation already used to test cosmic variance effects. We parametrise galaxy environments as done with data, in both the VIPERS-like and the reference mocks, and classify the LD and HD environments. The comparison indicates that our method is not harmed by the effects of the VIPERS design: in each VIPERS-like mock, the classification is in good agreement with the one obtained in the reference (i.e. working without the limitations of the observational strategy). About 70% of galaxies for which  $\delta$  is below the 25th (above the 75th) percentile in the reference mocks remain in the LD (HD) environment also in the VIPERS-like ones. For the purity, we considered the interlopers that should have been associated to LD or HD (according to the reference estimate) but erroneously fall in the opposite environments. We find that less than 8% of low-density galaxies in the reference are misclassified as high density in the VIPERS-like mocks, and a similar percentage of HD galaxies become LD interlopers.

## Appendix B: Volumes occupied by HD and LD galaxies

In this appendix we describe the technique of evaluating the comoving volumes where we recover the low- and high-density regions. Also in this case, we rely on the volume-limited sample introduced in Sect. 2.4, meaning those objects with  $M_B \leq -20.4 - z$  that have been used to estimate the galaxy density contrast  $\delta$ . Unlike a flux-limited one, such a sample has uniform characteristics from  $z = 0.5$  to  $0.9$  and should not introduce any redshift-dependent bias (Cucciati et al. 2014). We already know the local density contrast of these bright galaxies (Sect. 2.4), so we can identify the ones that belong to LD or HD environments (Sect. 3.1).

<sup>14</sup> The other mock catalogues, built according the semi-analytical model (see Sect. 5.1), are not used here because they cover a single sky region of  $7 \times 1 \text{ deg}^2$ .



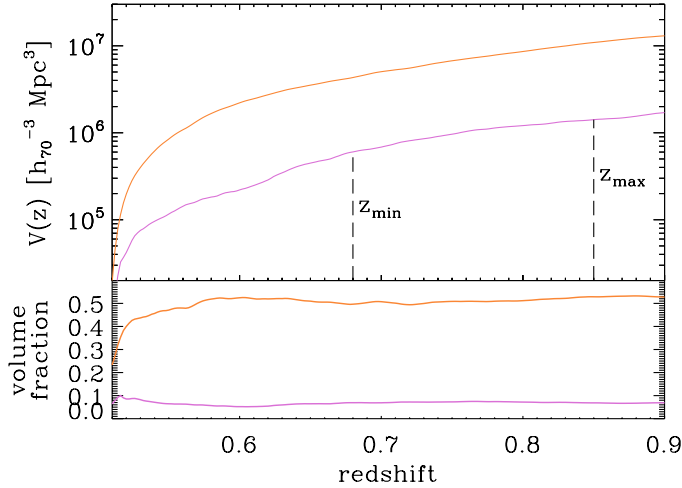


**Fig. B.1.** *Upper panel:* function of the comoving volume between redshift 0.51 and  $z$ , filled by either HD and LD regions (violet and orange lines). The function is evaluated by means of a Monte Carlo integration as described in the text. To find the  $V_{\max}$  of a galaxy, one has to consider the volume between its minimum and maximum allowed redshift ( $z_{\min}$  and  $z_{\max}$ , see the vertical dashed lines as an example). *Lower panel:* the fraction of the total volume (between  $z = 0.5$  and the given redshift) occupied by HD and LD regions (violet and orange lines).

We fill the whole VIPERS volume with random particles homogeneously distributed with a comoving density equal to  $2 h_{70}^3 \text{ Mpc}^{-3}$ . We associate each random particle to the nearest galaxy in the volume-limited sample. Particles linked to LD (HD) galaxies are taken into account to estimate the volume occupied by the LD (or HD) regions, which is the fraction of particles in the specific environment multiplied by the total VIPERS volume. Namely, this is a Monte Carlo integration in comoving coordinates (see e.g. Weinzierl 2000).

We compare this estimate to an alternative technique based on the Voronoi decomposition (e.g. Marinoni et al. 2002, and references therein). Around a chosen galaxy (belonging to the volume-limited sample), a Voronoi polyhedron is unambiguously defined as the set of points closer to that object than to any other. Once realised, such a partition of the VIPERS space, we add the polyhedra of LD/HD galaxies together to estimate the volume of the two environments. This sum overestimates the previous result by  $\sim 20\%$ , because a few Voronoi polyhedra exceed the effective volume of VIPERS, meaning that they expand in the VIMOS gaps. On the other hand, in the Monte Carlo integration, we do not deal with such a problem because we can easily remove random particles that fall out from the spectroscopic area. We verified that the two techniques are in excellent agreement for galaxies far from the survey gaps.

Once we have delimited low and high densities in 3D space, we plot the LD/HD volumes ( $V_{\text{LD}}$  and  $V_{\text{HD}}$ )<sup>15</sup> enclosed between  $z = 0.5$  and a certain  $z_{\text{up}}$ . This upper boundary runs from 0.5 to 0.9 with steps of  $\Delta z = 0.002$ . That is,

$$V_{\text{env}}(z_{\text{up}}) = \frac{N_{\text{env}}(0.5, z_{\text{up}})}{N(0.5, z_{\text{up}})} V(0.5, z_{\text{up}}), \quad (\text{B.1})$$

where  $N_{\text{env}}/N$  is the fraction of random particles – in the range  $[0.5, z_{\text{up}}]$  – associated with the given environment, while  $V$  is the comoving volume of the whole survey in the same redshift slice (see Fig. B.1). As said before,  $V$  is computed by considering only

<sup>15</sup> In the following we also refer to these volumes with the general term  $V_{\text{env}}$ .

the effective (i.e. spectroscopically observed) area of VIPERS, and the random particles outside of that are not considered. We linearly interpolate  $V_{\text{env}}(z_{\text{up}})$  between consecutive values of  $z_{\text{up}}$  to get a continuous function  $V_{\text{env}}(z)$ , shown in the upper panel of Fig. B.1.

When computing the GSMF (Sect. 4.1), we use  $V_{\text{env}}(z)$  to determine the  $V_{\max}$  volume. Each VIPERS galaxy is detectable between redshift  $z_{\min}$  and  $z_{\max}$ , i.e. the distances at which the object becomes respectively brighter/fainter than the flux range of the survey. In some cases  $z_{\min}$  and/or  $z_{\max}$  fall outside the  $z$ -bin in which the GSMF is measured. If so, we replace  $z_{\min}$  ( $z_{\max}$ ) with the lower (upper) limit of the bin. Once its redshift interval of observability has been established, the  $V_{\max}$  of a given galaxy is equal to  $V_{\text{env}}(z_{\max}) - V_{\text{env}}(z_{\min})$ , as illustrated in Fig. B.1. This approach is a variation of the method of Schmidt (1968), accounting for the spatial segregation of the sample. Indeed, the “classical” computation of  $1/V_{\max}$  is based on the area of the whole survey, while here we assume that galaxies contributing to the LD/HD stellar mass function cannot be observed outside their environment. With the exception of the first  $\sim 130 h_{70}^{-1} \text{ Mpc}$  along the line of sight (between  $z = 0.51$  and  $0.55$ ), the percentage of the total volume occupied by the HD and LD structures is nearly constant, i.e. about 7% and 50%, respectively (Fig. B.1, lower panel).

This technique could be also applied to the semi-analytic mock samples (Sect. 5.1), but in the present work we do not use it because of a few systematics that make the comparison to real data more difficult. One reason is that the cosmological parameters of the Millennium simulation (based on WMAP1, Spergel et al. 2003) could be different from the ones of the observed Universe. In particular, the amplitude of matter fluctuations on  $8 h^{-1} \text{ Mpc}$  scale should be overestimated in the simulation (where  $\sigma_8 = 0.9$ ) compared to more recent measurements ( $\sigma_8 \approx 0.8$ ). Also  $\Omega_{\Lambda}$ ,  $\Omega_{\text{m}}$ , and the spectral index of the primordial perturbation field are slightly different in WMAP1 from what is found by WMAP9 (Hinshaw et al. 2013) and Planck (Planck Collaboration XIII 2015). In view of these facts, the HD/LD thresholds in the model may not agree with data. Compared to VIPERS, low-density regions should be more extended, while the overdensities should be concentrated in a smaller volume, as expected in a more clustered Universe. These differences will be verified in future work.

Wang et al. (2008) investigated some consequences of varying cosmological parameters in a simulation. They ran the same SAM (De Lucia & Blaizot 2007) several times, but changed the cosmology from WMAP1 to WMAP3 (Spergel et al. 2007). The variations due to the new parameters mostly cancel out at  $z \sim 0$ , while they are significant at  $z \gtrsim 1$ . This is especially evident by looking at the GSMF (Wang et al. 2008, Fig. 14), which starts to overpredict the observations already at  $z = 0.5$  when WMAP1 parameters are assumed. The luminosity function is less affected by these systematics (Wang et al. 2008, Fig. 13). We also notice that modifications of the galaxy formation model should have less of an impact than cosmology on the GSMF.

We identified low- and high-density galaxies in the Wang et al. boxes ( $125 h^{-1} \text{ Mpc}$  comoving size), those based on WMAP1, as well as the boxes with WMAP3 cosmology. We observe that the distribution of the density contrast has a higher tail at high values of  $\delta$  when WMAP1 is the reference. Thus, the two thresholds that divide HD and LD regions are more extreme

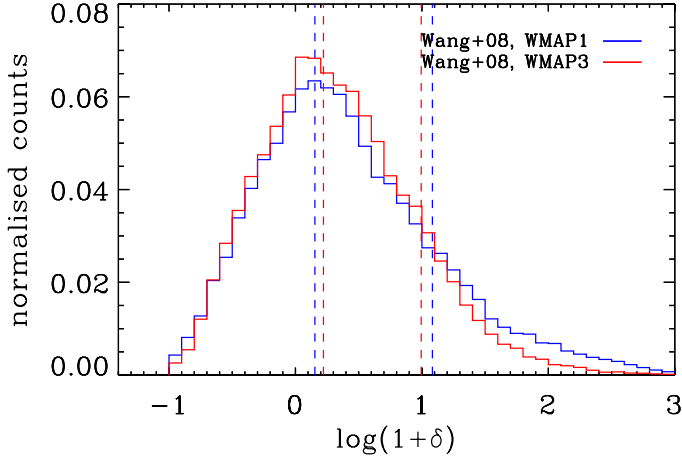


**Fig. B.2.** Distribution of  $1 + \delta$  in two cosmological boxes at  $z = 0.75$ . In both simulations, galaxies evolve according to De Lucia & Blaizot (2007) prescriptions. The cosmological parameters used as input are not the same, since taken from WMAP1 (red histogram) or WMAP3 (blue histogram). In this case, since we are not restricted to projected coordinates, we evaluated the density contrast using the 5NN in 3D space.

(Fig. B.2), mainly because structures form earlier in the WMAP1 case<sup>16</sup>.

The systematic effects are even more severe when comparing our mock samples (which are based on WMAP1) to observations: they are due not only to cosmology (especially  $\sigma_8$ ) but also to differences between modelled galaxies and real ones, because of both theoretical and observational limitations. For example, the luminosity function predicted by De Lucia & Blaizot (2007) at  $z \sim 0.7$  has a characteristic magnitude ( $M_B^* \simeq -20.5$ ) about 0.2 dex brighter than the one measured in VIPERS (Fritz et al. 2014). It means that galaxies with  $M_B < 20.4 - z$ , which is used to define the 5NN, has a higher number density and should trace the environment on slightly smaller scales. As an aside, we note that these outcomes suggest another possible use of our dataset: since they are sensitive to cosmological parameters, the reconstructed volumes from observations can be used to devise a new kind of cosmological test.

<sup>16</sup> Similar results are found by Guo et al. (2013) comparing WMAP1 and WMAP7 parameters. For example, at a fixed cosmic time massive haloes ( $> 10^{12.5} M_\odot$ ) are more abundant with a WMAP1 cosmology (Guo et al. 2013, Fig. 1).